49th AIAA Aerospace Sciences Meeting and Exhibit **AIAA-2011-1071**
Orlando, FL, 4-7 January 2011

Performance studies of the VASIMR® VX-200

Edgar A. Bering, III[1]
University of Houston, Department of Physics, Houston, TX 77204, USA

Benjamin W. Longmier[2], Maxwell Ballenger[3], Chris S. Olsen[4], Jared P. Squire[5], Franklin R. Chang Díaz[6]
Ad Astra Rocket Company, Webster, TX 77598, USA

Recent exhaust plume measurements and plasma physics results are discussed related to the development of the Variable Specific Impulse Magnetoplasma Rocket (VASIMR®) VX-200 engine, a 200 kW flight-technology prototype. Results from high power Helicon only and Helicon with ICH experiments are presented from the VX-200 using argon propellant. Total VX-200 system efficiencies are presented from recent results with greater than 100 kW of RF power, and extrapolation from an empirical fit shows greater than 60% efficiency at less than 200 kW RF power. A two-axis translation stage has been used to survey the spatial structure of plasma parameters, momentum flux and magnetic perturbations in the VX-200 exhaust plume. These recent measurements of axial plasma density and ambipolar potential profiles, magnetic field-line shaping, charge exchange, and force measurements were made within a new 150 cubic meter cryo-pumped vacuum chamber and are presented in the context of plasma detachment. Recent results at 200 kW coupled RF power have shown a thruster efficiency of 72% at a specific impulse of 5000 s and a thrust of 5.7 N.

Nomenclature

η_A	=	ICH coupler efficiency
η_b	=	ion coupling efficiency
f	=	frequency
f_{ci}	=	ion cyclotron frequency
F	=	ion velocity phase space distribution function
Γ_i	=	total ion flux
I_{sp}	=	specific impulse
L_A	=	inductance of the ICH coupler
L_M	=	inductance of the ICH coupler matching network
m_{doti}	=	mass flow rate
P_{plasma}	=	ICH RF power broadcast into plasma
P_{ion}	=	ICH RF power coupled into ions
P_{ICH}	=	ICH RF power into coupler
Q_c	=	quality factor of the ICH coupler circuit
R_c	=	resistance of the ICH coupler circuit
R_p	=	plasma loading of the ICH coupler
Θ	=	pitch angle
v_{ICRF}	=	exhaust plasma flow velocity with ICH on
$v_{helicon}$	=	exhaust plasma flow velocity with helicon only

[1] Professor, Physics and ECE, 617 Science & Research I /PHYS 5005, Associate Fellow
[2] Research Scientist, Ad Astra Rocket Company, 141 W. Bay Area Blvd.. and, formerly, ISSO Postdoctoral Aerospace Fellow, Department of Physics, University of Houston, Member
[3] Staff Scientist, Ad Astra Rocket Company, 141 W. Bay Area Blvd.
[4] Research Scientist, Ad Astra Rocket Company, 141 W. Bay Area Blvd.
[5] Vice President of Research, Ad Astra Rocket Company, 141 W. Bay Area Blvd., Member.
[6] Chief Executive Officer, Ad Astra Rocket Company, 141 W. Bay Area Blvd., Associate Fellow.

$VSWR_{plasma}$ = voltage standing wave ratio of the ICH coupler, with plasma present
$VSWR_{vacuum}$ = voltage standing wave ratio of the ICH coupler, with no plasma present
W_{ICH} = mean ion energy increase owing to ICH
ω = angular frequency

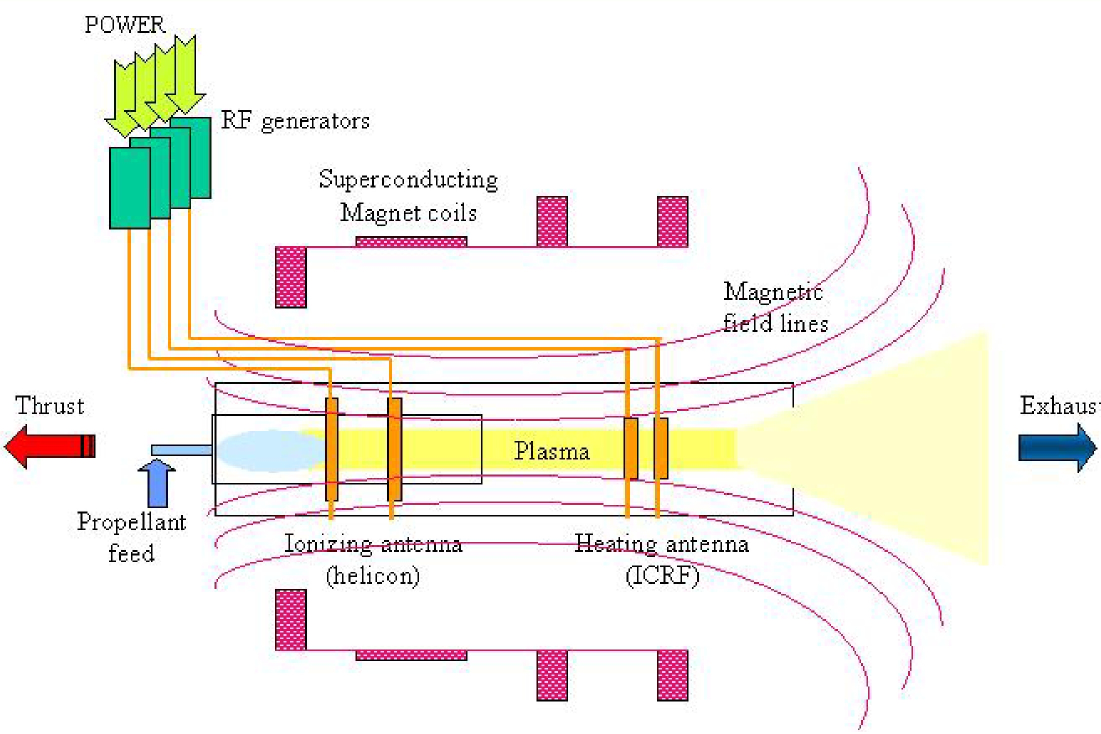

Figure 1. Cartoon block diagram of the VASIMR™ system, illustrating the basic physics.

I. Introduction

THE exploration of the solar system will be one of the defining scientific tasks of the new century. One of the obvious challenges faced by this enterprise is the scale size of the system under study, 10^{11} - 10^{14} m. Over distances on this scale and given the performance of present day rockets, the mission designer is faced with the choice of accepting multi-year or even decadal mission time lines, paying for enormous investment in rocket propellant compared to useful payload, or finding a way to improve the performance of today's chemical rockets. For human space flight beyond Earth's orbit, medical, psychological, and logistic considerations all dictate that drastic thruster improvement is the only choice that can be made. Even for robotic missions beyond Mars, mission time lines of years can be prohibitive obstacles to success, meaning that improvements in deep space sustainer engines are of importance to all phases of solar system exploration[1].

Better thruster performance can best be achieved by using an external energy source to accelerate or heat the propellant[2,3]. High-power electric propulsion thrusters can reduce propellant mass for heavy-payload orbit-raising missions and cargo missions to the Moon and near Earth asteroids and can reduce the trip time of robotic and piloted planetary missions.[1,4,5,6] The Variable Specific Impulse Magnetoplasma Rocket (VASIMR®) VX-200 engine is an electric propulsion system capable of processing power densities on the order of 6 MW/m^2 with a high specific impulse and an inherent capability to vary the thrust and specific impulse at a constant power. The potential for long lifetime is due primarily to the radial magnetic confinement of both ions and electrons in a quasi-neutral flowing plasma stream, which acts to significantly reduce the plasma impingement on the walls of the rocket core. High temperature ceramic plasma-facing surfaces handle the thermal radiation, the principal heat transfer mechanism from the discharge. The rocket uses an optimized helicon plasma source[7,8] for efficient plasma production in the first stage. This plasma is energized further by an ion cyclotron heating (ICH) RF stage that uses left hand polarized slow mode waves launched from the high field side of the ion cyclotron resonance. Useful thrust is produced as the plasma accelerates in an expanding magnetic field, a process described by conservation of the first adiabatic invariant as the magnetic field strength decreases in the exhaust region of the VASIMR®.[9,10,11] This paper will

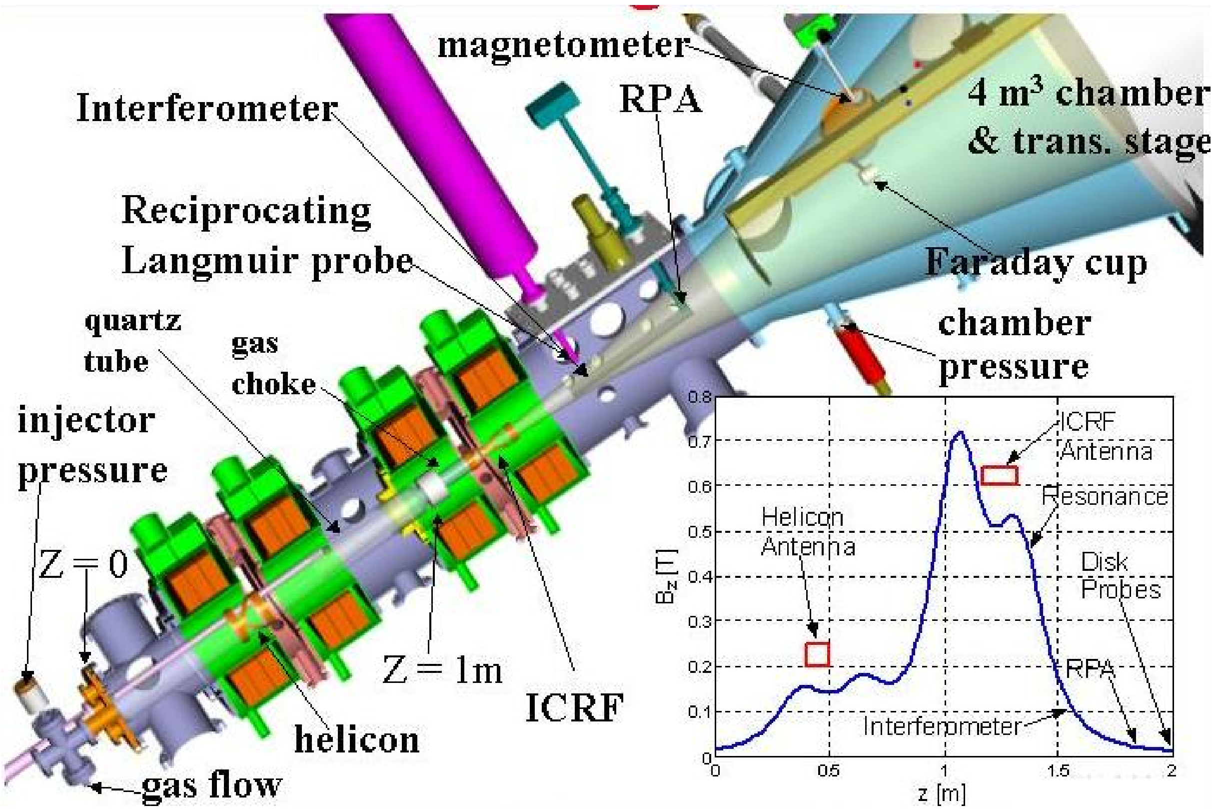

Figure 2. Cutaway trimetric engineering drawing of the present configuration of the VASIMR™ VX-50.

discuss an experimental investigation of the use of Ion Cyclotron Heating (ICH) to provide an efficient method of electrodeless plasma acceleration in the VASIMR® engine. Particular emphasis in this paper will be placed on investigation of the spatial structure of the exhaust plume and recent advances in system performance.

Research on the VASIMR® engine began in the late 1970's, as a spin-off from investigations on magnetic divertors for fusion technology[12]. A simplified schematic of the engine is shown in Figure 1. The VASIMR® consists of three main sections: a helicon plasma source, an ICH plasma accelerator, and a magnetic nozzle[3,13,14,15,16,17]. Figure 2 shows these three stages integrated with the necessary supporting systems. One key aspect of this concept is its electrode-less design, which makes it suitable for high power density and long component life by reducing plasma erosion and other materials complications. The magnetic field ties the three stages together and, through the magnet assemblies, transmits the exhaust reaction forces that ultimately propel the ship.

The plasma ions are accelerated in the second stage by ion cyclotron resonance heating (ICH), a well-known technique, used extensively in magnetic confinement fusion research[18,19,20,21,22]. Owing to magnetic field limitations on existing superconducting technology, the system presently favors light propellants. However, the helicon, as a stand-alone plasma generator, can efficiently ionize heavier propellants such as argon and xenon.

An important consideration involves the rapid absorption of ion cyclotron waves by the high-speed plasma flow. This process differs from the familiar ion cyclotron resonance utilized in tokamak fusion plasmas as the particles in VASIMR® pass through the coupler only once[17,23,24,25]. Sufficient ion cyclotron wave (ICW) absorption has nevertheless been predicted by recent theoretical studies[26], as well as observed and reported in various conferences and symposia.

Elimination of a magnetic bottle, a feature in the original VASIMR® concept, was motivated by theoretical modeling of single-pass absorption of the ion cyclotron wave on a magnetic field gradient[24]. While the cyclotron heating process in the confined plasma of fusion experiments results in approximately thermalized ion energy distributions, the non-linear absorption of energy in the single-pass process results in a boost, or displacement of the ion kinetic energy distribution. The ions are ejected through the magnetic nozzle before thermal relaxation occurs.

Natural processes in the auroral region may also exhibit a related form of single pass ICH. “Ion conic” energetic ion pitch angle distributions are frequently observed in the auroral regions of the Earth's ionosphere and

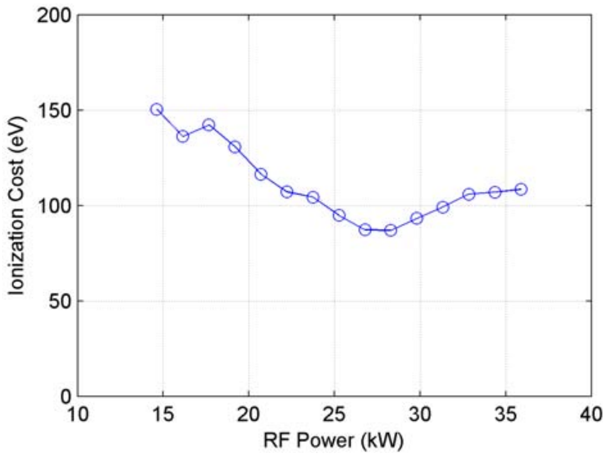

Figure 3. Minimum ionization cost is now 87 ± 9 eV/ion.

magnetosphere[27,28,29,30,31,32,33]. It is not relevant to list the entire range of models that have been proposed to account for these observations. Many models propose wave-driven transverse ion acceleration followed by adiabatic upwelling of the distribution[34,35 and references therein]. Proposed driver wave modes include current driven electrostatic ion cyclotron (EIC) waves[36,37,38], and electromagnetic ion cyclotron waves[39,40,41], among others. Other mechanisms proposed include interaction with an oblique double layer or dc potential structure[42,43]. The fact that ion conics are commonly found on auroral field lines suggests that transverse ion acceleration is a ubiquitous process in auroral arcs[35]. Space-borne observations of narrow-band ion-cyclotron waves with unambiguous spectral peaks near the ion cyclotron frequencies are relatively rare[44,45,46,47,48,49,50,51,52]. Most studies have found that the most common wave phenomenon found in association with transverse ion acceleration is broad-band ELF noise[35,53,54,55,56]. All of these authors suggest that current driven EIC waves make up some or all of the broad-band ELF noise, but they are unable to prove it, even when wavelength measurements are available[47,48]. The role of inhomogenieties or shear in reducing the threshold for current-driven EIC instability is suggested as one solution to this problem[48,57]. EMIC waves appear to be associated with transverse ion acceleration ~10% of the time[35,41].

In addition to the extensive body of work on the heating of magnetic confinement fusion plasmas that was superficially cited above, there is a thirty year body of theoretical and laboratory work on transverse ion acceleration by current driven EIC modes[34,36,43,58,59]. All of these experiments have typically used current driven EIC waves, parametric decay of lower hybrid waves, or other mode conversion process to launch the required wave field. Direct injection, which is used in VASIMR®, requires the coupler to have good plasma loading in order to launch the waves with useful efficiency, as discussed below. Since the magnetospheric simulation experiments have aimed at simulating EIC driven heating and VASIMR® uses EMIC waves, these prior results have limited application to the VASIMR®. What has been shown of relevance is that acceleration followed by adiabatic folding is a viable mechanism for producing ion conics[34,59]. However, the field ratios employed were an order of magnitude smaller that used in the VASIMR® studies reported here.

VASIMR® has a transverse ion acceleration stage or booster that uses EMIC waves, followed by adiabatic expansion. Simultaneous ambipolar acceleration is also observed in the VASIMR® exhaust plume that may be interpreted as a large-scale double layer[60]. Thus, VASIMR® results may be of interest to proponents of more than one model of ion conic production.

The VASIMR® engine has three major subsystems, the plasma generator stage, the RF “booster” stage and the nozzle, shown in Figures 1 and 2[16]. Laboratory physics demonstrator experiments (VX-50 and VX-100) were developed and tested first at the NASA Johnson Space Center for several years and more recently at the Ad Astra Rocket Company[61,62]. The details of the engine and its design principles have been previously reported[17,63]. The first stage is a helicon discharge that has been optimized for maximum power efficiency (lowest ionization cost in eV/(electron-ion pair) [,64,65,66,67]. The next stage downstream is the heating system. Energy is fed to the system in the form of a circularly polarized rf signal tuned to the ion cyclotron frequency. ICH heating has been chosen because it transfers energy directly and largely to the ions, which maximizes the efficiency of the engine[11,12]. In the present small-scale test version, there is no mirror chamber and the ions make one pass through the ICH coupler. The system also features a two-stage magnetic nozzle, which accelerates the plasma particles by converting their azimuthal energy into directed momentum. The detachment of the plume from the field takes place mainly by the loss of adiabaticity and the rapid increase of the local plasma β, defined as the local ratio of the plasma pressure to the magnetic pressure.

After 10 years of growth and improvement, the VX-50 had achieved all of the physics test goals that could reasonably be obtained. In October, 2006, the VX-50 was decommissioned and disassembled. In its place, the Ad Astra Rocket Company has built two new machines, the VX-100, which is a laboratory physics demonstrator test bed, and the VX-200, which is a flight-like prototype. The VX-100, a new test bed for the VASIMR® plasma engine, developed by Ad Astra Rocket Company, achieved record performance tests conducted at the company's old Houston laboratory in 2007. The VX-100 test facility, which went into operation in late January of 2007, began to yield reliable experimental data in early February of 2007 and was operated until October 2007.

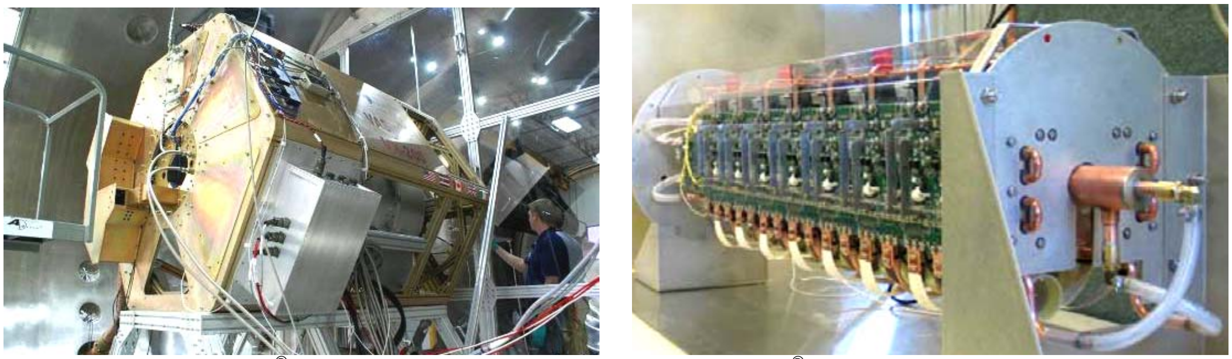

Figure 5. (a) VASIMR® VX-200i prototype. (b) VASIMR® VX-200i and VX-200 solid-state RF amplifier, 1m in length.

The VX-200 is a 200kW VASIMR® engine prototype currently in the early stages of the testing phase. The VX-200, completed in May of 2009, is considered by company officials to be the last step before construction of the VF-200 (for VASIMR® flight) series of flight engines planned for space testing in 2013.

The VX-100 and the VX-200 both demonstrated ionization costs below 100 eV/ion (Figure 3). The ionization cost is a measure of the engine's plasma production efficiency with values below 100 being required to ensure efficient operation. Recent tests have focussed on the VASIMR® VX-200 ICH second stage.

For the first time, end-to-end testing of the VX-200 engine has been undertaken with an optimum magnetic field and in a vacuum facility with sufficient volume and pumping to permit exhaust plume measurements at low background pressures. Experimental results are presented with the VX-200 engine installed in a 150 m^3 vacuum chamber with an operating pressure below $1x10^{-2}$ Pa ($1x10^{-4}$ Torr), and with exhaust plume diagnostics over a range of 5 m in the axial direction and 1 m in the radial directions. Measurements of plasma flux, RF power, and neutral argon gas flow rate, combined with knowledge of the kinetic energy of the ions leaving the VX-200 engine, are used to determine the ionization cost of the argon plasma. A plasma momentum flux sensor (PMFS) measures the force density as a function of radial and axial position in the exhaust plume. New experimental data on ionization cost, exhaust plume expansion angle, thruster efficiency and total force are presented that characterize the VX-200 engine performance above 100 kW. A semi-empirical model of the thruster efficiency as a function of specific impulse has been developed to fit the experimental data. Recent results at 200 kW DC input power yields a thruster efficiency of 72% at a specific impulse of 5000 s and thrust of 5.7N.

a) 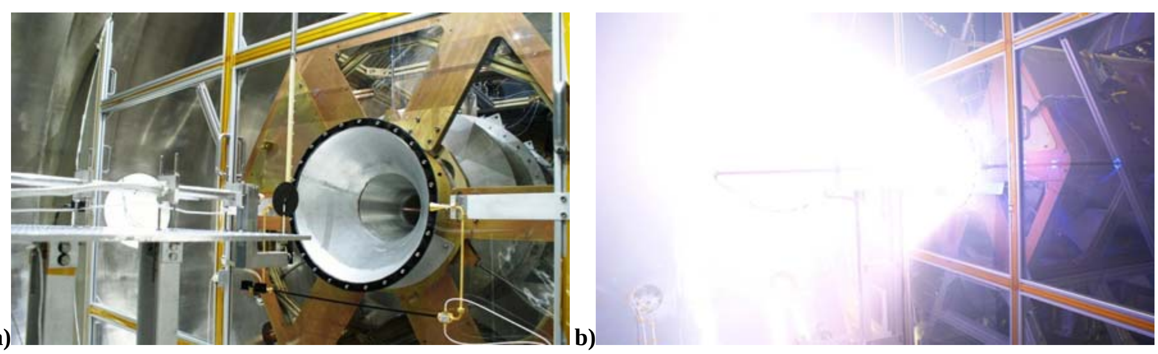 b)

Fig 4. Photograph of the VX-200 rocket exhaust end facing the diagnostics platform (a), and a high power firing of the VX-200 with immersed plasma diagnostics at closest approach (b).

II. Experimental Setup

A. The VASIMR® Engine

1. VX-200 and supporting hardware

The VX-200 has a total RF power capability of 200 kW driven by high-efficiency, as high as 98%, solid-state DC-RF generators, as shown in Figure 5b. The helicon plasma source of the VX-200 is driven at 35 kW using 25-150 mg/s of argon gas.. The helicon source internal structure was electrically floating.

The new Ad Astra Rocket Company vacuum chamber is 4.2 m in diameter with a total internal volume of 150 m^3, Figures 6a and 6b, and has four 50,000 l/s cryopanels for a total pumping capability of 200,000 l/s. The vacuum chamber is partitioned into two sections, a rocket section and an exhaust section. The rocket section stays at a space-like vacuum pressure which is lower than the exhaust section while the VX-200 is firing. Also shown in Figure 6b is a 2.5 m by 5 m translation stage that carries a suite of plasma diagnostics for plume characterization. The translation stage uses 2 independent ball screws and is driven by vacuum compatible stepper motors which yield a positional resolution of 0.5 mm. A vertical member mounted to the translation stage holds a mounting table. Each diagnostic is bolted directly to the mounting table for precise alignment and positioning on the translation stage. The red solid line in Figure 6a depicts the full axial range of possible plasma measurements. The red line extends into the VASIMR® VX-200 device, but does not penetrate the helicon source itself, and extends 5 m downstream into the expanding plume region of the vacuum chamber.

a)

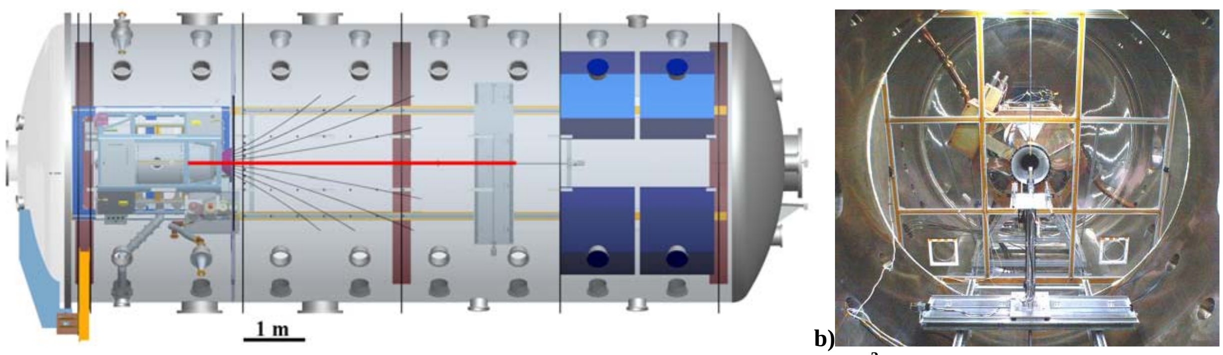

Figure 6. A CAD rendering of the VX-200 rocket bus mounted within the 150 m^3 Ad Astra Rocket Company high vacuum facility with superimposed vacuum magnetic field lines (a), and a photograph of the VX-200 rocket (background) and diagnostics platform (foreground) mounted on a 2 m by 5 m translation stage (b).

B. Diagnostics

Plasma diagnostics include a triple probe, 32 and 70 GHz density interferometers, a bolometer, a television monitor, an H-α photometer, a spectrometer, neutral gas pressure and flow measurements, several gridded energy analyzers (retarding potential analyzer or RPA)[3,16,68,69,70,71,72,73,74], a momentum flux probe[75], an emission probe, a directional, steerable RPA and other diagnostics[76]. Two 10-probe arrays of fixed bias flux probes and a density interferometer are the primary plasma diagnostics. The flux probe arrays measure ion current profiles. They are calibrated by the density interferometer. An array of thermocouples provides a temperature map of the system.

Measurements of the plasma potential, electron temperature and ion density in the VX-200 and VX200i rocket core and the plasma plume were made with a ¼" diameter tungsten Langmuir probe with a guard ring, Figure 8. The probe was swept in voltage from -40 V to +40 V through the entire range of ion saturation and electron saturation regions with a sweep rate of 80 Hz and a sampling rate of 40 kHz. RF compensation was tested, and produced only 0.2 V variations in the measured plasma potential, and 0.1 eV variations in the electron temperature. Floating potential measurements were made with a high impedance oscilloscope from 1 Hz to 100 MHz. Fluctuations in the floating potential were observed to have a maximum peak-to-peak amplitude of 0.4 V at the driving frequency of the helicon plasma source, near the industrial standard 6.78 MHz. Figure 9 shows a photograph of the argon exhaust plume produced by the helicon source from the VX-200. The translation stage and plasma diagnostics can be seen in the background of the photograph.

1. Retarding potential analyzer (RPA)

Retarding potential analyzer (RPA) diagnostics have been installed to measure the accelerated ions. Measurements of the ion energy in the downstream section of the VX-200 plume were made with a cylindrical 4 2-layer grid RPA mounted on powered goniometric hinge on the translation stage, to enable pitch angle scans. A four-grid configuration is used, with entrance attenuator, electron suppressor, ion analyzer and secondary suppressor grids. The grids were 49.2-wire/cm molybdenum mesh, spaced 1 mm apart with Macor spacers. The opening aperture is 1 cm in diameter, usually pointed at the plasma beam, mounted 0.1778 m from the center of the translation stage mounting table. For the results reported here, the VX-200 RPA did not have a front face collimator plate mounted.

a) 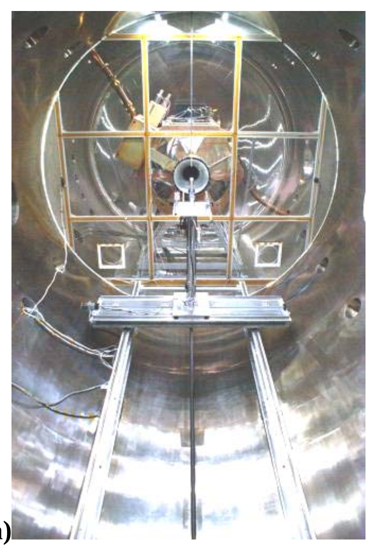

b) 

Figure 7. Photograph from within the Ad Astra Rocket Company vacuum chamber showing the translation stage, a), and VX-200i mounted within the vacuum chamber, b).

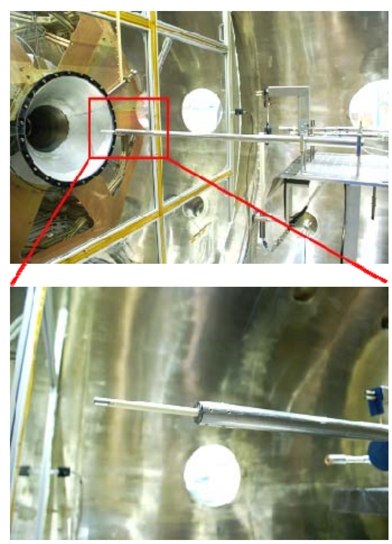

Figure 8. Photograph of a Langmuir probe with guard ring on a 70 cm extension shaft.

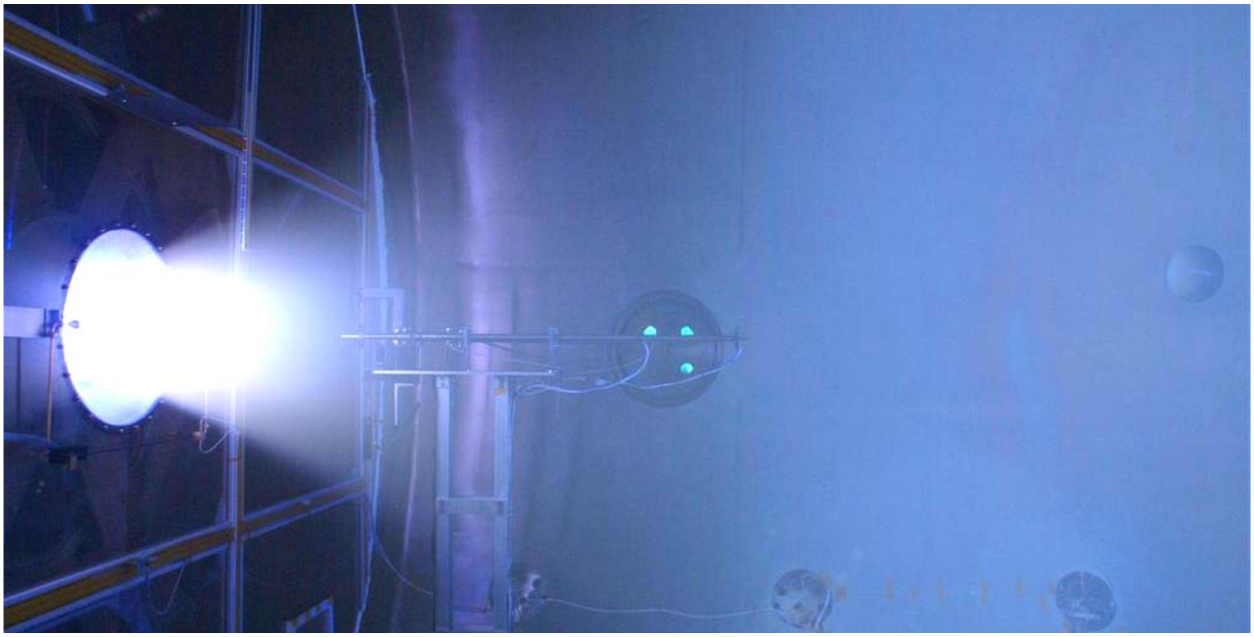

Figure 9. Photograph of the VX-200i exhaust plume with the translation stage and plasma diagnostics in the background.

The interpretation of RPA output data in terms of ion energy requires an accurate knowledge of plasma potential (V_p). When available, data from an rf compensated swept Langmuir probe provided by Los Alamos National Laboratory (LANL) are used to determine V_p. When other V_p data are not available, plasma potential is assumed to be the value at which *dI/dV* first significantly exceeds 0, which usually agreed with the LANL probe value within the error bars (±5 V). This value was typically ~+0-50 V with respect to chamber ground in the VX-50. The operator biases the body and entrance aperture of the RPA to the observed plasma potential value. The ion exhaust parameters are deduced from the raw data by means of least squares fits of drifting Maxwellians to the current-voltage data[67,69,72,77].

In this paper, the RPA data will be presented in several formats, including the voltage derivative of the I-V characteristic, the one-D ion velocity distribution function, a planar cut through the full ion velocity distribution function, and as derived parameters. The *dI/dV* plots (e.g. Figure 25) show the smoothed, numerically calculated derivative with respect to sweep voltage of the measured RPA current. Sweep voltage zero is set to plasma potential found using the methods of the previous paragraph, for ICH-off conditions and all other parameters unchanged. Unless stated otherwise, seventy-eight sweeps per shot of the RPA have been averaged to produce each VX-200 figure. The presence of features in the *dI/dV* curves at retarding voltages less than the plasma potential are the result of temporal fluctuations in the ion saturation current, and largely serve to illustrate the risks in taking numerical derivatives of data. The ion velocity distribution functions (e.g. Figure 27) were found from the *dI/dV* curves by dividing by the energy and multiplying by a calibration factor.

The RPA I-V characteristic data has been reduced by least-squares fitting the characteristic that would be produced by a drifting Maxwellian to the data. This fit has three parameters. The three free parameters in these fits are ion density, mean drift speed and the parallel ion temperature in the frame of reference moving with the beam. The temperature is found from these least squares fits, not from taking the slope of the logarithm of the data. The density is calibrated by comparison with nearby Langmuir probes and is probably best understood as a relative measurement. The temperature and ion drift speed parameters depend most strongly on the accuracy with which the retarding potential is known. The absolute uncertainty of the sweep voltage digitization with respect to chamber ground was a few percent when digitizer calibration uncertainty, sweep isolator reduction ratio precision and related parameters are folded in. There are systematic uncertainties associated with the determinations of plasma potential, which are discussed two paragraphs above. Plasma potential is always subtracted prior to any other analysis.

The full ion velocity phase space distribution function of the ions can be obtained by scanning the RPA in pitch angle between otherwise identical shots, assuming cylindrical (gyrotropic) symmetry[78,79]. The angle step size was 5º from 0º to 50º and 10º thereafter for all contour plot figures (Figure 19).

C. Concept and Construction of the PMFS

The PMFS was developed and constructed based on a previous NASA-Marshall Space Flight Center design. The PMFS consists of a 9-centimeter-diameter graphite target disc attached to a 10-centimeter-long insulating alumina rod. The stiff alumina rod then connects to a small titanium bar (5.72 cm x 1.30 cm) where a series of 4 high output semiconductor strain gauges are mounted between two holes on an 'isthmus' on the titanium bar, as seen in Figure 10. The isthmus acts as a stress concentrator and increases the sensitivity of the device. The strain gauges are connected electrically in a Wheatstone bridge configuration so that changes in temperature of the titanium bar do not affect the linearity of the strain gauge output. When the graphite disc is immersed in flowing plasma (e.g. the exhaust plume of VASIMR or Hall thruster) the force from the plasma impacting the graphite target is translated into a strain in the titanium beam through a moment arm equal to the length of the alumina rod plus the clamp length. A small graphite shield was also used to keep the entire titanium bar and strain gauge assembly shielded from the flowing plasma, and associated thermal and electrical noise.

The resolution of the PMFS is 0.1 mN, which allowed for sufficiently sensitive measurements of the force applied by the exhaust plasma. In a series of Hall thruster experiments in 2007, an average discrepancy between the measured force from the PMFS and the measured force from the University of Michigan thrust stand of approximately 2% was observed, indicating a good agreement between the two force measurement techniques. For reference, the typical error associated with the inverted pendulum thrust stand is ±2 mN for a measured force of 100 mN, indicating that the typical 2% difference observed between the two force measurement techniques is usually within the error associated with the thrust stand.

The same PMFS that was calibrated at the University of Michigan is now mounted on the translations stage in the VX-200 exhaust plume measurements. The PMFS graphite paddle also served to shield the 3-axis magnetometer alumina housing from the direct impact of the plasma exhaust plume. PMFS data were obtained on virtually every plasma shot during the major campaigns described in this paper. Data were digitized at 40 kHz.

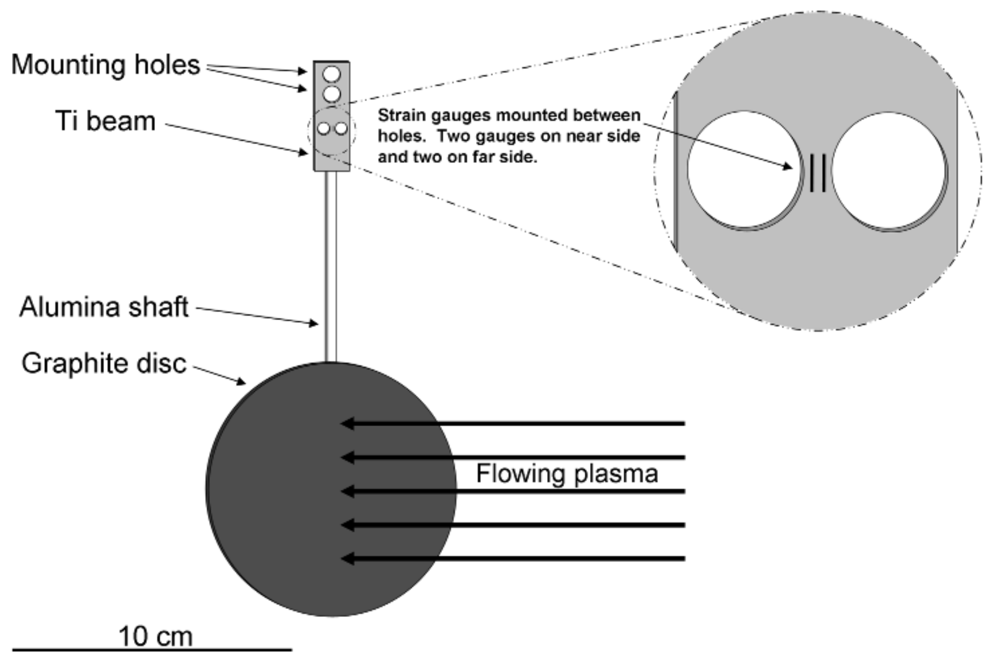

Figure 10. Schematic of the PMFS assembly and zoom in of strain gauge arrangement mounted on the Ti isthmus.

If an increased force resolution were required, the length of the alumina moment arm could be increased, acting to increase the output from the strain gauges for a particular force applied to the graphite target. However, increasing the arm length of the device also decreases the resonant frequency response. This limitation is generally not a concern for steady-state thruster operation. If the thruster (or some other source of flowing plasma) were operated in a pulsed mode, then data analysis is simplified if the moment arm was selected such that the natural period of the PMFS device is much shorter than the thruster pulse duration.

The diameter of the graphite targets used in Hall thruster and VX-200 experiment campaigns was smaller than the diameter of the Hall and VX-200 thruster plume, therefore the target only measured a portion of the total force generated by the Hall and VX-200 thrusters in each measurement. The PMFS target diameter was 50% of the P-5 thruster channel O.D. An azimuthally integrated radial profile of the ion flux was used to account for the portion of the plasma plume that was not intercepted by the graphite target. For each force measurement presented in this paper, a corresponding radial profile of the ion flux was collected and used to determine the total force produced by the thruster.

The ratio of the total ion flux (r=0 to r=100 cm), numerically integrated over the entire plume assuming cylindrical symmetry, to that of the ion flux intercepted by the graphite target (r=0 cm to r=9 cm) is given by

$$\frac{\sum_{x=0}^{x=1000} \pi\left(r_{\mathrm{x+1}}^2 - r_{\mathrm{x}}^2\right) I\left(r_{\mathrm{x}}\right)}{\sum_{x=0}^{x=90} \pi\left(r_{\mathrm{x+1}}^2 - r_{\mathrm{x}}^2\right) I\left(r_{\mathrm{x}}\right)} \tag{1}$$

where $I(r_{\mathrm{x}})$ is the ion current as measured by a Faraday probe biased into ion saturation at a radius r_{x} in the plasma exhaust. Here, *x* ranges from 0 to 1,000 for r_{x} values from 0 to 100 cm.

The total force, F_{Total}, produced by the Hall thruster is determined by multiplying the force measured by the graphite target, F_{Target}, by Eqn. (1), which becomes

$$F_{\mathrm{Total}} = F_{\mathrm{Target}} \frac{\sum_{x=0}^{x=1000} \pi\left(r_{\mathrm{x+1}}^2 - r_{\mathrm{x}}^2\right) I\left(r_{\mathrm{x}}\right)}{\sum_{x=0}^{x=90} \pi\left(r_{\mathrm{x+1}}^2 - r_{\mathrm{x}}^2\right) I\left(r_{\mathrm{x}}\right)} \tag{2}$$

Charge-exchange (CEX) particles and doubly-charged ions do not affect the accuracy of the PMFS as long as the fraction of these CEX neutrals and doubly-charged ions is small compared to singly-charged ions, or the CEX and doubly-ionized fluxes are directly proportional to the ion flux. This is a reasonable assumption based on previous data taken with the P5 Hall Thruster.[17]

The assumption that the thruster plume is symmetric in the azimuthal direction leads to the largest source of error with the PMFS device. One way to reduce this error is to construct a 2-D map of the ion flux profile; this mapping was performed only in the VX-200 case. In the Hall thruster series of experiments it was found that assuming azimuthal symmetry led to no larger than a 5.7% difference between the force measured by the PMFS and the inverted pendulum thrust stand, and typically resulted in no more than a 2% difference.

Once a total force measurement was numerically integrated from the PMFS measurement and ion flux profile, momentum reflection and sputtering were taken into consideration and corrections were made[75].

III. Experimental Momentum Flux Results

A. VX-200 Momentum Flux Measurements

The VX-200 achieved full rated operating power of 200 kW dc power in to the ICH rf transmitters on Sept. 30, 2009. During the last year, several experiment campaigns have mapped the exhaust plume and characterized the output of the thruster. Thruster overall performance is in a preliminary stage, and additional major improvements are planned. Thus, all results reported here must be regarded as preliminary.

Contour maps of the momentum flux density in the exhaust plume of the VX-200 are shown in Figures 11 and 12. These maps were constructed by interpolating the PMFS data taken on a regular 10 cm grid during separate plasma shots. The origin of the *z* (or axial) coordinate is the edge of the end cap vacuum flange. The end of the motor nozzle is at 2.6 m on this scale. Several major points stand out in these figures. The helicon only plume produces orders of magnitude more force than a neutral gas jet with the same mass flow rate. The ICH increases the force level by a factor of at least 5. The boundary of the plume is essentially a straight line. This pattern is taken as evidence that the exhaust plume is detaching from the magnetic field. Finally, the thrust density falls off exponentially with distance from the nozzle. The e-folding distance of this decay is consistent with the charge exchange mean free path owing to resonant charge exchange with the neutral background that builds up in the chamber during each shot. Thus, this fall-off is a laboratory effect that will not occur in flight.

The sharply collimated nature of the thrust and plasma in the exhaust plume were further studied by constructing a comparison plot of the thrust density and ion flux data taken on one of the innermost radial scans (z = 2.9 m). Cylindrical symmetry was assumed. The results have been plotted in a trimetric wire frame view shown in Figure 13. Two features stand out. The inner core of the ion flux is sharply peaked, with a shoulder at about $r \sim 0.15$ m. The thrust density profile is broader in the center than the flux density, but then falls off more steeply at the edge. This columnar geometry is required for high nozzle efficiency and is consistent with plasma detachment. The cause of the shoulder in the flux profile is unknown and under investigation.

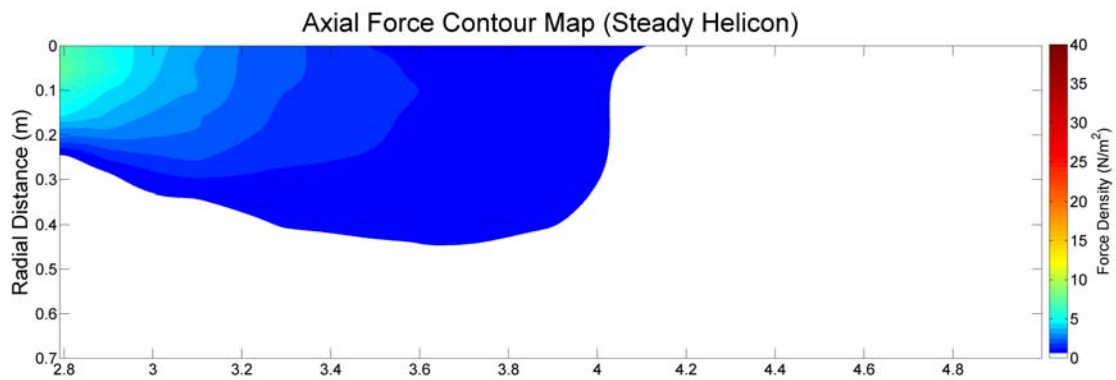

Figure 11. VX-200 helicon plume map based on data from the PMFS graphite target. Exact units are intentionally left off pending further calibration. Data were taken over several radial passes of the 2 axis translation stage. The first stage Helicon discharge produces noticeable force above a low flow neutral gas jet.

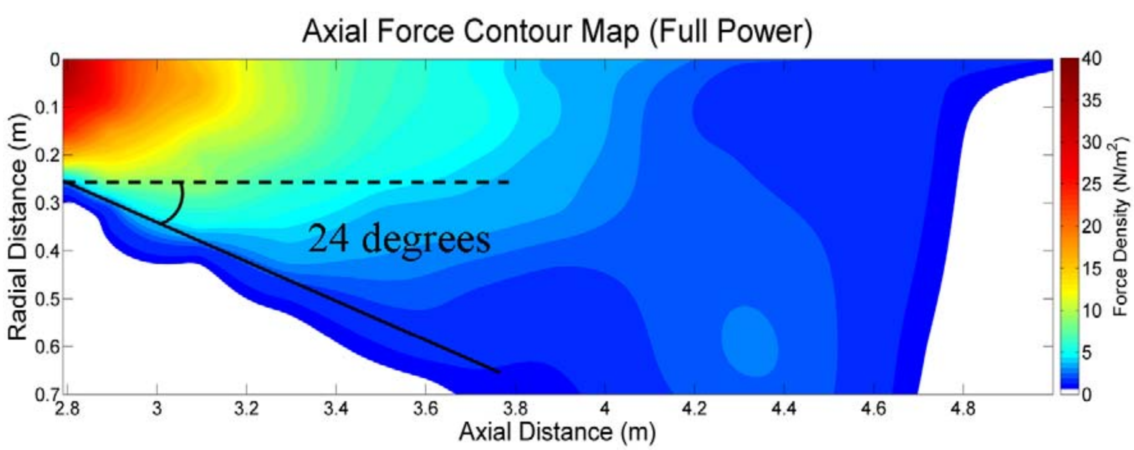

Figure 12. VX-200 full power plume map based on data from the PMFS graphite target. Exact units are intentionally left off pending further calibration. The data in this figure were taken approximately 3 s after the data in Figure 15. The peak force increases by a factor of 5 with the addition of approximately 145 kW of RF power. This demonstrates that the momentum flux in the plume of the VASIMR® is well defined and directed downstream of the rocket engine.

IV. General VX-200 Results

A. Power Data

As noted above, the VX-200 achieved design full power operation on Sept. 30, 2009. New high power records were set on November 19, 2010. The total rf power delivered to the plasma by rf amplifiers during the record high power shot is shown in Figure 14. The ICH amplifier was on from 0.3 to 1.2 s. The stepped turn-on ramp reflects the modular design of the amplifier and the modular sequencing of the turn-on process. The ability of the VX-200 to sustain high power operations for extended time intervals is demonstrated in Figure 15. The figure shows that the ICH amplifier operated at 161 kW for 5 s. As presently configured, the main factors preventing continuous steady state operation are the melting point of certain glues used in the engine core and limited pumping capacity . Figure 15 demonstrates that the rf system is capable of sustained high power operation.

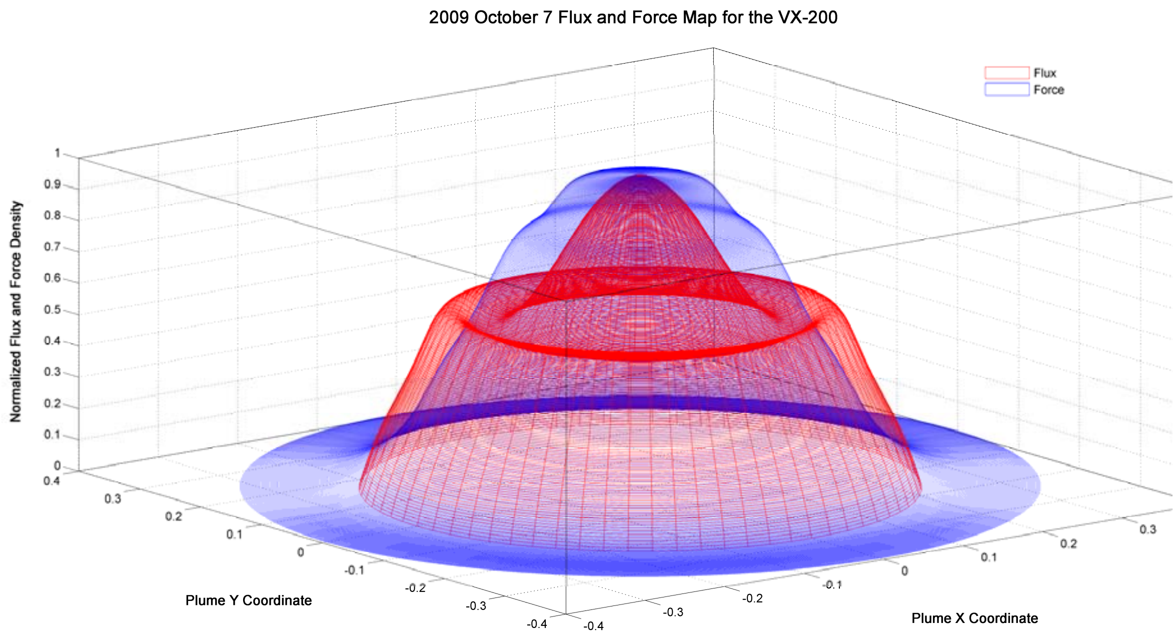

Figure 13. Force density (blue) and ion flux data from a *z* = 2.9 m radial scan are plotted in a trimetric view of plume structure assuming cylindrical symmetry.

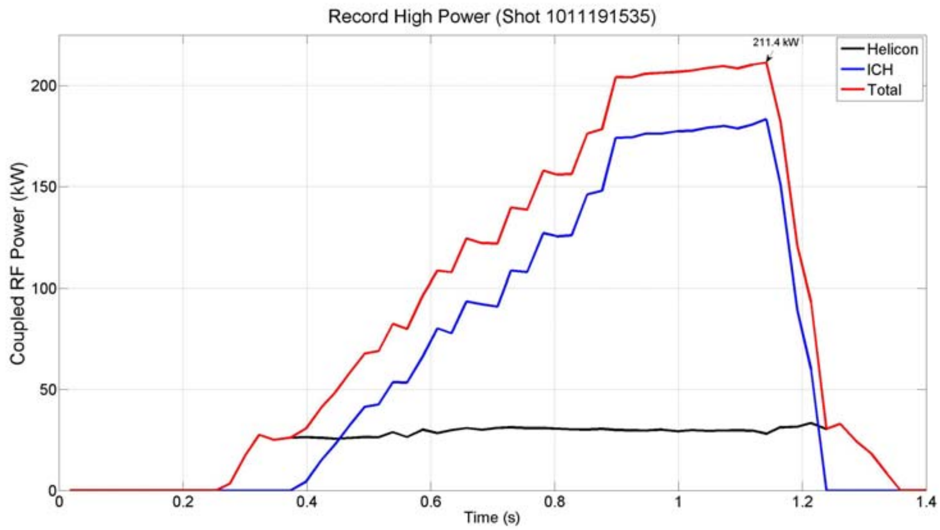

Figure 14. Total RF power coupled to the plasma by the VASIMR rf amplifiers plotted as a function of time during the record full power shot. The helicon amplifier operated at 28 kW, and the ICH amplifier peaked at 183 kW.

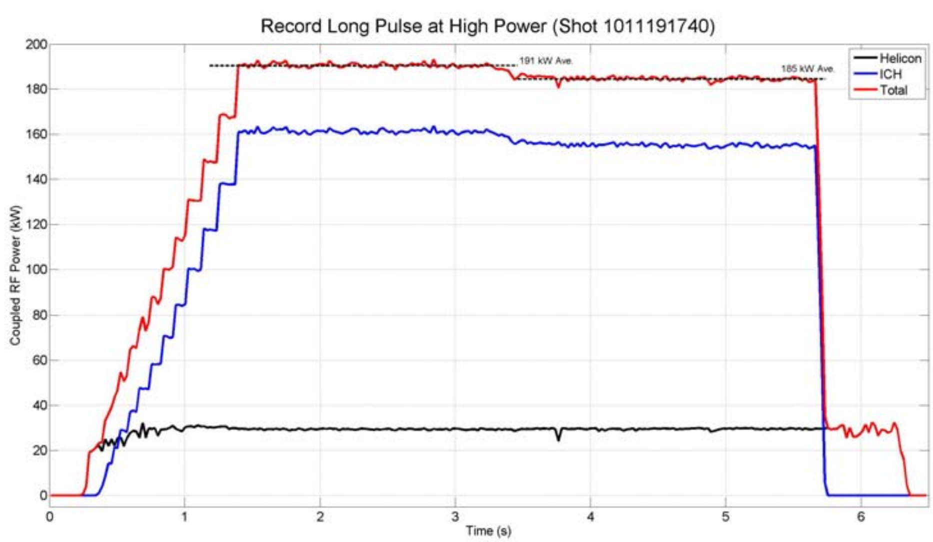

Figure 15. Total power curve for a shot where ICH operation was sustained for >5 s.

B. Plasma Data

Ion flux maps of the VX-200 plasma plume are shown in Figures 16 and `17. The contour maps are based on planar Langmuir probe data taken in one location per plasma shot. An extended campaign of a week's duration was required to make 10-cm step radial scans at several axial distances. Contour maps were constructed using standard 2-D interpolation techniques. Two points stand out. First, the plume has a sharp, relatively straight outer boundary,

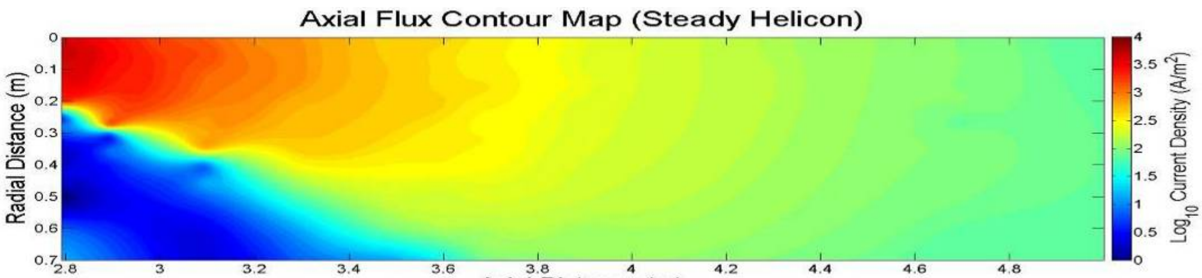

Figure 16. VX-200 ion flux map (first stage Helicon only) based on Langmuir Probe data. The small planer molybdenum probe was steadily biased into ion saturation (- 30 V). The plume is slightly asymmetric and the ions are affected by charge exchange.

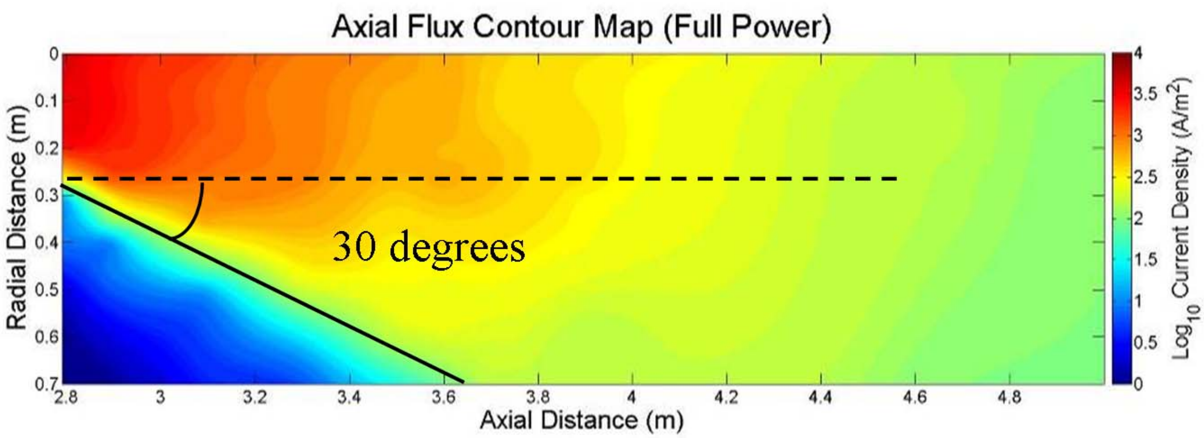

Figure 17. VX-200 ion flux map (Full power Helicon and ICRF) based on Langmuir probe data. The data in this figure are taken approximately 3 seconds after the data from Figure 17. The plume is slightly broader than with Helicon only as well as better defined along the edges. More ion flux propagates downstream despite a higher exhaust chamber pressure since the increased ion energy corresponds to a larger charge exchange mean free path.

which we take to indicate that the plasma plume is detaching and not following magnetic field lines. Second, the ICH plume extends further downstream than the helicon only plume, which appears to show a greater charge exchange mean free path for the higher energy ions. The pressure data indicate that the charge exchange mean free path was ~100-120 cm.

The ICH boost is intended to provide an efficient method of accelerating the ions. This acceleration is misnamed "heating." The process is deterministic and affects only one degree of freedom. The effect of the ICH on the ions in the VX-200 is in explored in Figures 18-20. Figure 18 shows a trimetric wireframe view of the ion energy distributions from the RPA located on the centerline at z = 2.9 m, plotted as a function of both ion energy and ICH power, all normalized. The ion energy increases from a peak at ~50 eV produced by the helicon plus ambipolar acceleration to ~180 eV at full ICH power. This level is lower than intended for the VF-200, owing to deliberate, temporary use of a sub-optimal ICH coupler for initial tests. There was also a residual low energy peak, indicating that either that charge exchange was acting to produce a low energy, cool ion population or that the only part of the ion population was accelerated.

Figure 19 shows a comparison of contour plots of the 2-D ion velocity phase space distribution function for ICH on vs ICH off. These data were obtained in a discharge with an argon flow rate of ~3000 sccm, 29 kW of helicon

RF, and 94 kW ICH on and ICH off. Data were taken at 5 radii from 0 to 40 cm from the centerline at z = 3.893 m (1.293 m from nozzle). The black arrows in the color contour plots show B. The red arrows indicate where the data were taken in reference to a schematic of the 10 m x 4.2 m vacuum chamber with the VX-200 engine, RF generators, RF power measurement location, vacuum partitioning wall, representative magnetic field lines, and the measurement range of the exhaust plume diagnostics. These data were taken 1.5 m downstream from the ICH resonance. The measurements were made using the powered angle scan mount of the RPA, moving the translation stage so as to keep the RPA in one place. These figures show three things. First, the accelerated ion jet is tightly collimated in velocity space. Second, at this distance, the unaccelerated component shows evidence of a substantial amount of elastic scattering to higher pitch angles. Third, the off axis figures indicate that the jet had a substantial axial component, even as far as 40 cm off axis. Some ions are still flowing along B, but a substantial fraction can be seen to be flowing in an axial direction, which indicates that magnetic detachment was occurring.

Figure 20 shows the fit parameters inferred by least squares fitting drifting Maxwellians to the RPA I-V characteristics: parallel ion temperature in the frame of the beam, drift velocity, and an uncalibrated parameter corresponding to density. Panel (a) shows an axial scan, with the RPA at a radius of -0.178 m. Panel (b) shows a diameter scan at $z = 3.6$ m. The VASIMR nozzle exit is located at $z = 2.6$ m. Two striking things jump out of this figure. The density decays exponentially, with an e-folding distance of 1.2 m, which is consistent with charge exchange as the loss mechanism. The apparent ion acceleration near the nozzle may be ambipolar acceleration. However, it is probably the result of the location of the RPA off the centerline. At the closest distances, it was in the fringe of the plume.

V. Efficiency

For the first time, the total force from the VASIMR VX-200 engine has been measured. The operating pressure was below 1×10^{-2} Pa (1×10^{-4} Torr) for data taken during 30 s long firings and was below 1×10^{-3} Pa (1×10^{-5} Torr) for the first 800 ms of each firing. Using the PMFS the force density within the exhaust plume of the VX-200 engine was measured as a function of the radial and axial position. To determine the total force produced by the VX-200 engine, the force density over one full radius of the exhaust plume, as shown in Fig. 21, was integrated using azimuthal symmetry. As the coupled RF power was increased from 28 kW to 108 kW, the total force produced by the VX-200 engine was measured using the PMFS. As shown in Figure 22, the total force measured increased with increasing ICH coupled RF power as expected.

For the data presented in Fig. 21 and Fig. 22 the PMFS was located at z=40 cm , where $E_{\parallel}/E_{\perp} = 98\%$. The PMFS was 9 cm in diameter; small compared to the total exhaust plume diameter of approximately 70 cm. The force density data for Fig. 21 was taken at 14 samples/cm radially from r=0 cm to r=40 cm, and 1 sample every 10 cm axially from z=40 cm to z=150 cm. The VX-200 engine was operated with 107 mg/s of Ar propellant, a peak magnetic field strength of 2 tesla, a helicon coupled RF power level of 28 kW and an ICH coupled RF power level of 90 kW for the data presented in Fig. 21, and an ICH power level range of 0 kW to 81 kW for the data presented in Fig. 22

No indication of secondary (ArIII) or tertiary (ArIV) ionization states were observed based on optical spectrometer measurements 30 cm downstream of the VX-200 engine exit plane. This implies that the population of ArIII and ArIV ions is at least less than 1% of the ArII population. For the data presented in Fig. 21, the ion-neutral charge exchange mean free path was 10 cm, and for Fig. 22 and Fig. 23, it was 100 cm.

Measurements of the ionization cost, defined as the ratio of the coupled RF power to the total ion current that is extracted from the system in the exhaust section, were taken during helicon-only operation as a function of both coupled RF power and argon propellant flow rate, from 15 kW to 35 kW and 50 mg/s to 150 mg/s respectively. The lowest ionization cost measurement of 87±9 eV occurred with VX-200 engine settings of 28 kW coupled RF power and 109 mg/s argon flow rate (Figure 3). The ionization cost term, E_i, appears in Eqn 7.

The ion current density and force density were mapped over a large region of the exhaust plume, more than 2 m axially and 1 m radially, with the flat faces of the ion current density probes and the PMFS always in a plane orthogonal to the VX-200 engine axis, i.e. always facing in the direction parallel to the engine axis. This mapping was performed at a total coupled RF power level of 90 kW and a neutral background pressure of 1×10^{-2} Pa (1×10^{-4} Torr). The plasma jet data exhibited a well defined edge in both ion current density and force density.[80] similar to other helicon based devices.[81] Assuming azimuthal symmetry, the conical boundary contour that surrounded 90% of the integrated ion current density and force density was calculated. The angle of that boundary line relative to the VX-200 engine axis, θ, provided an estimate of the exhaust divergence half-angle. The ion current density data yielded a divergence half-angle of 30±2 degrees (Fig. 17), while the force density data yielded a divergence half-angle of 24±2 degrees (Fig. 12). The half angles were found by radially integrating the ion current density and force density to 90% of the total ion current and total force. These radial maps of ion current density and force density were made between z=40 cm and z=150 cm at 10 cm intervals from the plane of the VX-200 engine exit. The ion flux probe and the PMFS were not rotated such that the ions impacted normal to these surfaces, but were left facing in the direction parallel to the VX-200 engine centerline and translated radially. The conical nozzle correction factor[82] can be used to estimate the fraction of directed momentum to total flow momentum. Here, this correction factor is defined as the nozzle efficiency when expressed as a percentage.

$$\eta_n = \frac{1}{2}(1 + \cos\theta) \tag{3}$$

The integrated current density and force density data yield a nozzle efficiency of 93% and 96% respectively. For the following system efficiency analysis, the more conservative 93% nozzle efficiency was used. This estimate was consistent with particle trajectory modeling[83] that predicted a nozzle efficiency of 90%. Calculations based on a MHD theory[84] that factors in possible drag effects due to the plasma leaving the high magnetic strength zone yield a nozzle efficiency of 87%.

The total thruster efficiency, η_T, of the VX-200 engine was determined by dividing the total RF power coupled to the plasma by the thruster jet power, where the jet power is defined as

$$P_{jet} = \frac{F^2}{2\dot{m}} \tag{4}$$

where F is the total force produced by the rocket and $\dot{m}$ is the total mass flow rate of propellant. Dividing equation 4, by the total RF power coupled to the plasma yields

$$\eta_T = \frac{P_{jet}}{P_{1,RF} + P_{2,RF}} \tag{5}$$

where $P_{1,RF}$ and $P_{2,RF}$ represent the RF power coupled to the helicon and ICH stages of VX-200 engine respectively. The May 2010 data presented in Fig. 23 used a propellant flow rate of 107 mg/s, a helicon coupled RF power level of 28 kW, and an ICH coupled RF power level from 0 to 81 kW which yielded results that show a total force of up to 3.6±0.2 N, an I_{sp} of 3400 s, and a 56% thruster efficiency. A retarding potential energy analyzer (RPA) was used to verify the PMFS results and reported a mean ion flow velocity of 32.8 km/s with an ion temperature of 24 eV in the frame of reference moving with the beam. Using the propellant mass flow rate of 107 mg/s, the RPA measurements indicate a total force of 3.5±0.5 N, within the error bars of the PMFS measurement. The specific impulse was calculated using the total force measurement and a propellant mass flow rate measurement where

$$I_{SP} = \frac{F}{\dot{m}g} \tag{6}$$

In the most recent campaign, in November. 2010, the thrust from sustained full power design operation was measured for the first time. The 200 kW shots shown in Figure 23 had a thruster efficiency of 72% at a specific impulse of 5000 s and thrust of 5.7N, at 120 mg/s. of Ar

The Helicon stage was operated at a constant 28 kW coupled RF power, while the ICH stage coupled RF power was varied from 0 to 183 kW, Fig 14 . Any change to the thruster efficiency was due largely to the increasing component of ICH coupled RF power. The limiting factor in the maximum ICH coupled RF power to the VX-200 engine was a vacuum pressure limit within the vacuum chamber, where greater RF circuit voltages produced glow or arc discharges that prompted the VX-200 engine solid state RF generators to shut down. The efficiency in Fig. 3 increases as a function of coupled ICH RF power and I_{sp}, indicating that the process of ICH wave coupling into the plasma column has not saturated.

A semi-empirical model of the thruster efficiency[80,85,86] for VX-200 engine, Eqn. 5, is also shown in Fig. 3, and is a least squares fit to the data using the ICH coupling efficiency as the only free parameter, such that

$$\eta_T = \frac{\frac{1}{2} m_{Ar} g^2 I_{sp}^2}{eE_i + eE_1\left(1 - \frac{1}{\eta_B}\right) + \frac{\frac{1}{2} m_{Ar} g^2 I_{sp}^2}{\eta_B \eta_n}} \tag{5}$$

Where m_{Ar} is the atomic mass of argon, e is the electron charge, E_i is the ionization cost of the propellant, E_1 is the first stage RF power coupled to the ions that is converted into directed kinetic energy through ambipolar acceleration, and η_B is the ICH efficiency. The ionization cost of the propellant was 87±9 eV/ion-extracted, the kinetic energy of ions leaving the first stage was 12±1 eV, and the nozzle efficiency was 93%. The only free parameter is the second stage coupling efficiency, η_B, which was fit to the data using a least squares algorithm, and was found to be 74%. It should be noted that η_B also includes the efficiency loss due to the ion energy spread in the exhaust, i.e. the frozen flow losses due to the finite ion temperature. Decreasing E_i or increasing E_1 shifts the semi-empirical model curve to the left and increasing η_B or η_N shifts the curve upward. The VX-200 engine helicon and ICH couplers were designed to produce a thruster efficiency of 60% at 5000 s using 200 kW DC input power (equivalent to 186 kW of coupled helicon and ICH RF power). The measured thruster efficiency shows that the VX-200 engine achieves a thruster efficiency of 72% at 5000 s using ~200 kW of coupled RF power.

VI. Conclusions

The VX-200 is now operating with superconducting magnets and has achieved full design power. The plasma exhaust plume of the VX-200 has properties and structure that demonstrate that the VX-200 is approaching full design performance. The geometry of the plume is consistent with the occurrence of plasma detachment. The plasma is moving ballistically and does not appear to be following the magnetic field lines. Neutral gas build-up is observed to reduce charge exchange mean free path to ~ 1 m. For the first time, the thruster efficiency and thrust of a high-power VASIMR® prototype have been measured with the thruster installed inside a vacuum chamber with sufficient volume and pumping to simulate the vacuum conditions of space. Using an ion flux probe array and a plasma momentum flux sensor (PMFS), the exhaust of the VX-200 engine was characterized as a function of the coupled RF power and as a function of the radial and axial position within the exhaust plume. A thruster efficiency of 72% was calculated using the force measurements and propellant flow rate with the specific impulse of 5000 s when operating at a total RF coupled power of 200 kW. The ionization cost of argon propellant was determined to be 87 eV for optimized values of RF power and propellant flow rate. This work paves the way for design and eventual operation of the VASIMR® in orbit on-board the ISS.

Acknowledgments

The authors (B.L.) would like to thank the University of Houston Institute for Space Systems Operations (ISSO) postdoctoral fellowship program for partial support of this research. NASA Johnson Space Center under grant NAG 9-1524, the Texas Higher Education Coordinating Board under Advanced Technology Program project 003652-0464-1999 and the Ad Astra Rocket Company sponsored this research.

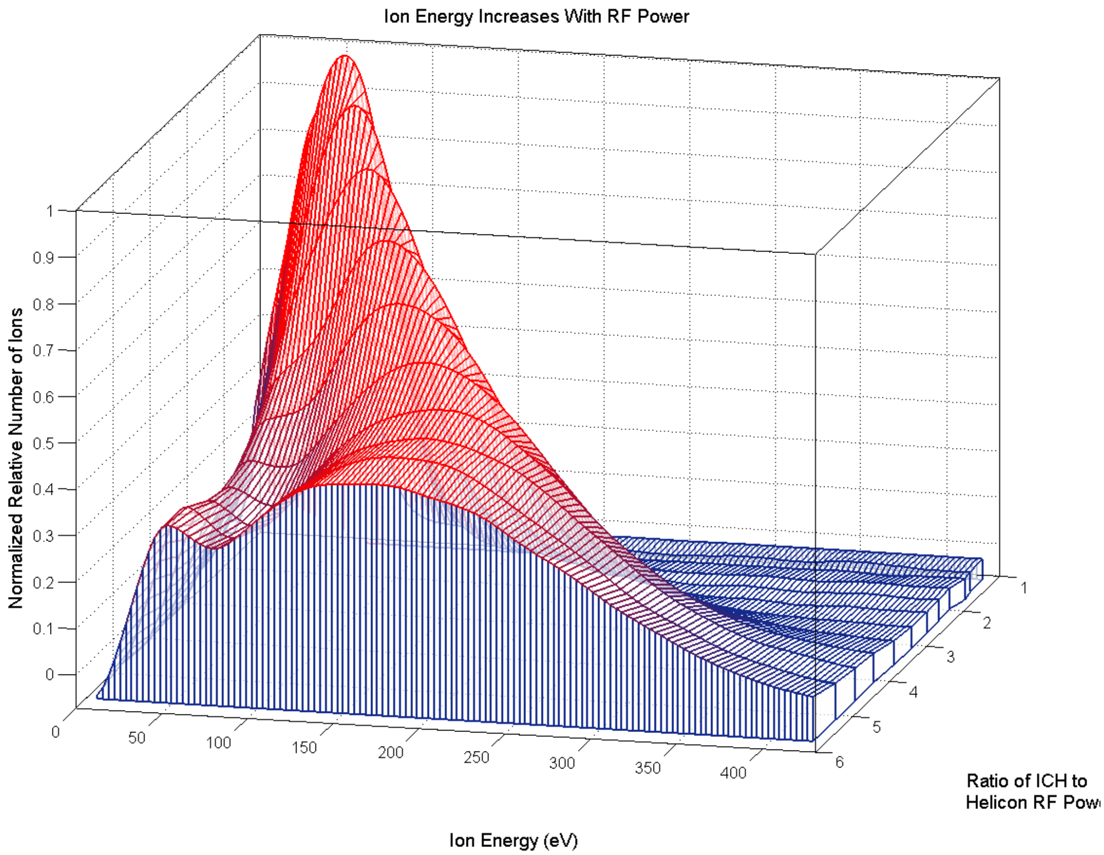

Figure 18. Ion energy distribution function measured by the RPA at an axial distance *z* = 2.9 m, showing a trimetric wire-frame view of the evolution of the ion energy distribution as ICH power increases.

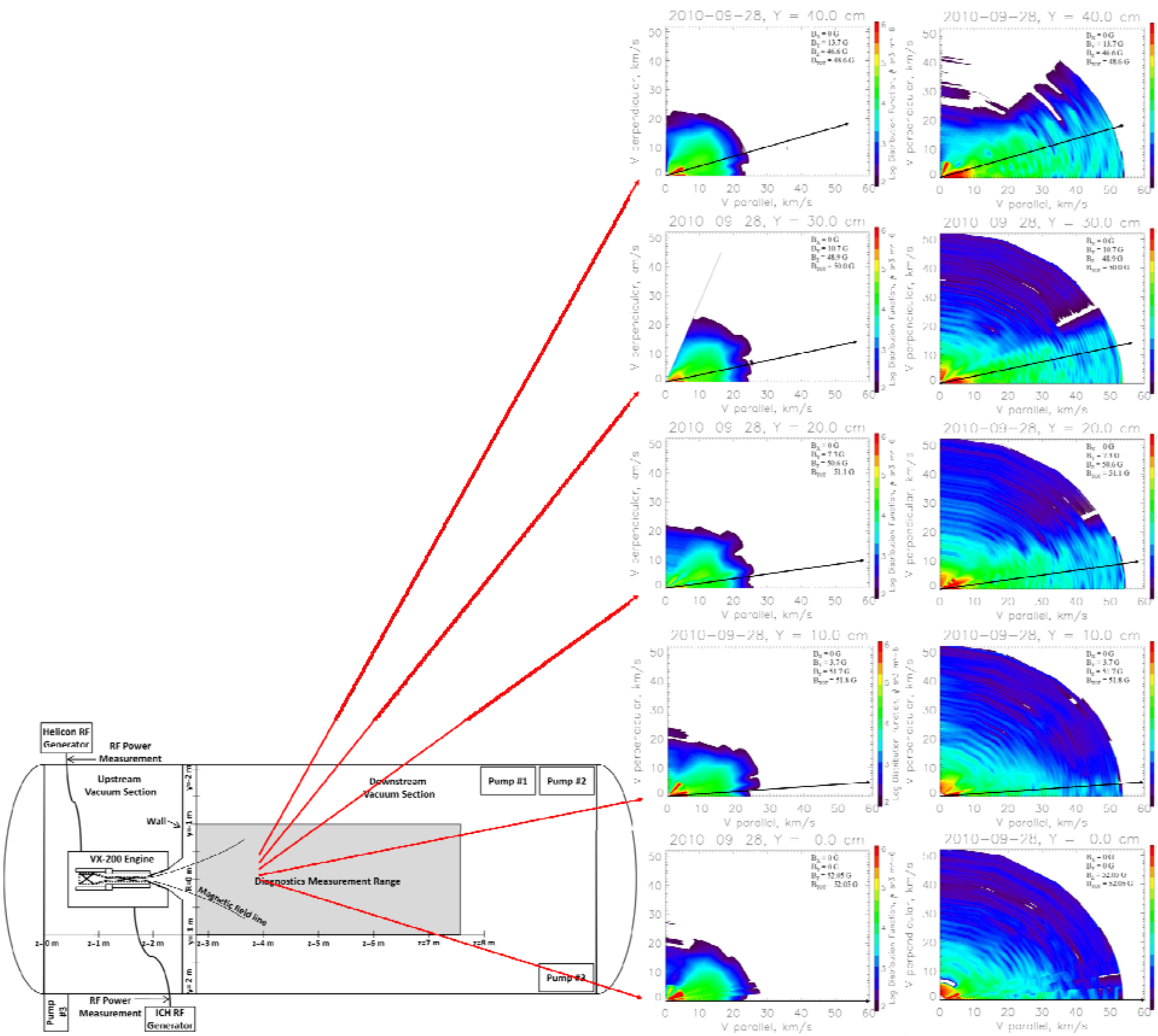

Figure 19 Ion velocity phase space distribution functions, in a discharge with an argon flow rate of ~3000 sccm, 29 kW of helicon RF, and 94 kW ICH on and ICH off. Data were taken at 5 radii from 0 to 40 cm from the centerline at z = 3.893 m (1.293 m from nozzle). Black arrows show B. red arrows indicate location data were taken on a schematic of the 10 m x 4.2 m vacuum chamber with the VX-200 engine, RF generators, RF power measurement location, vacuum partitioning wall, representative magnetic field lines, and the measurement range of the exhaust plume diagnostics.

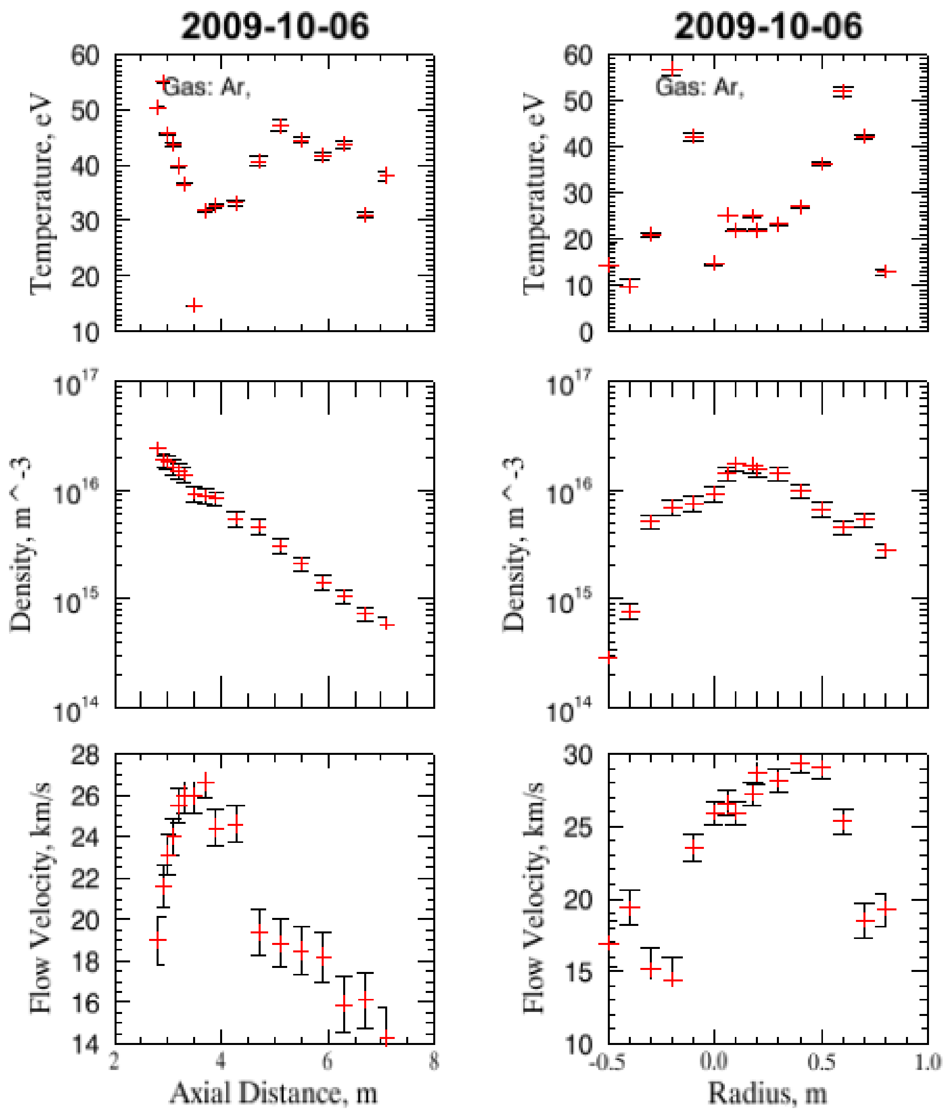

Figure 20. Parameters inferred from least squares fitting a drifting Maxwellian to RPA data. From top to bottom, panels show parallel ion temperature in the frame of the beam, ion density (uncalibrated, arbitrary units) and ion flow velocity. (a) Axial plot. Origin of the *z*-axis is at the edge of the upstream end of the vacuum chamber. Motor nozzle is at z = 2.6 m. All data were taken with the RPA at y = -0.178 m when stage $y = 0$. (b) Radial plot. RPA is on center at y = 0.178 m. This diameter scan was at $z = 3.6$ m.

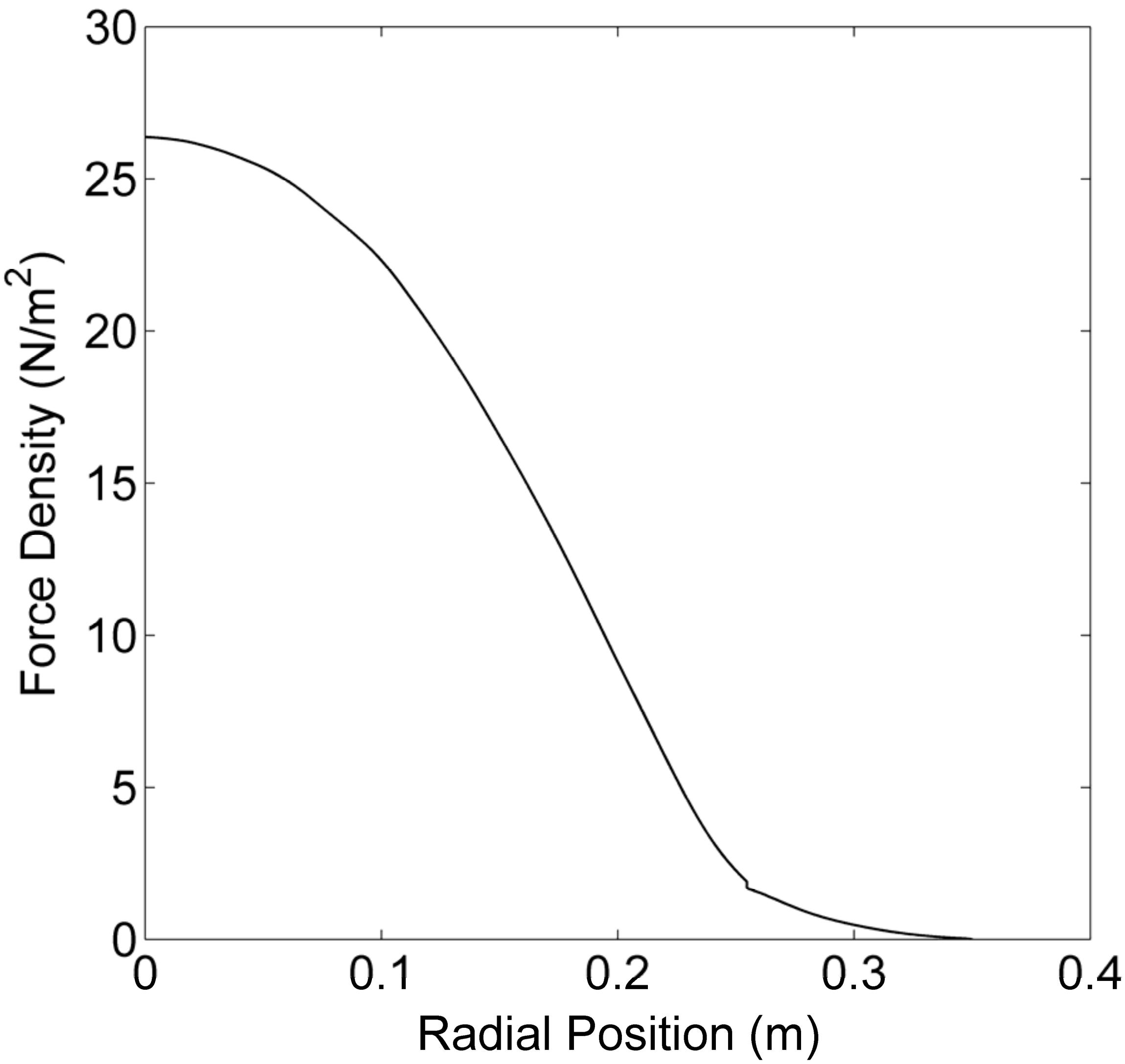

Figure 21. A measured radial profile of the VX-200 engine force density. Error is 7% of the force density value.

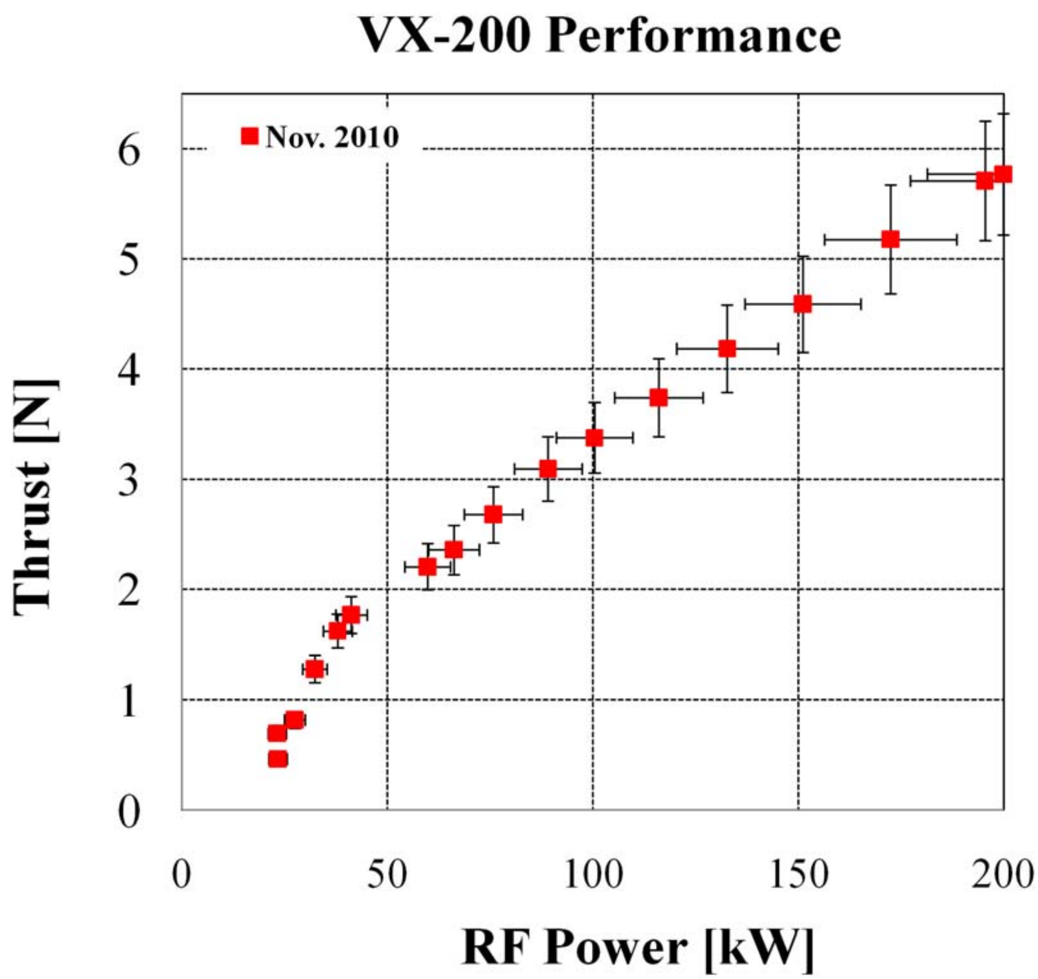

Figure 22. The total force of the VX-200 engine as a function of the RF power coupled to the argon plasma.

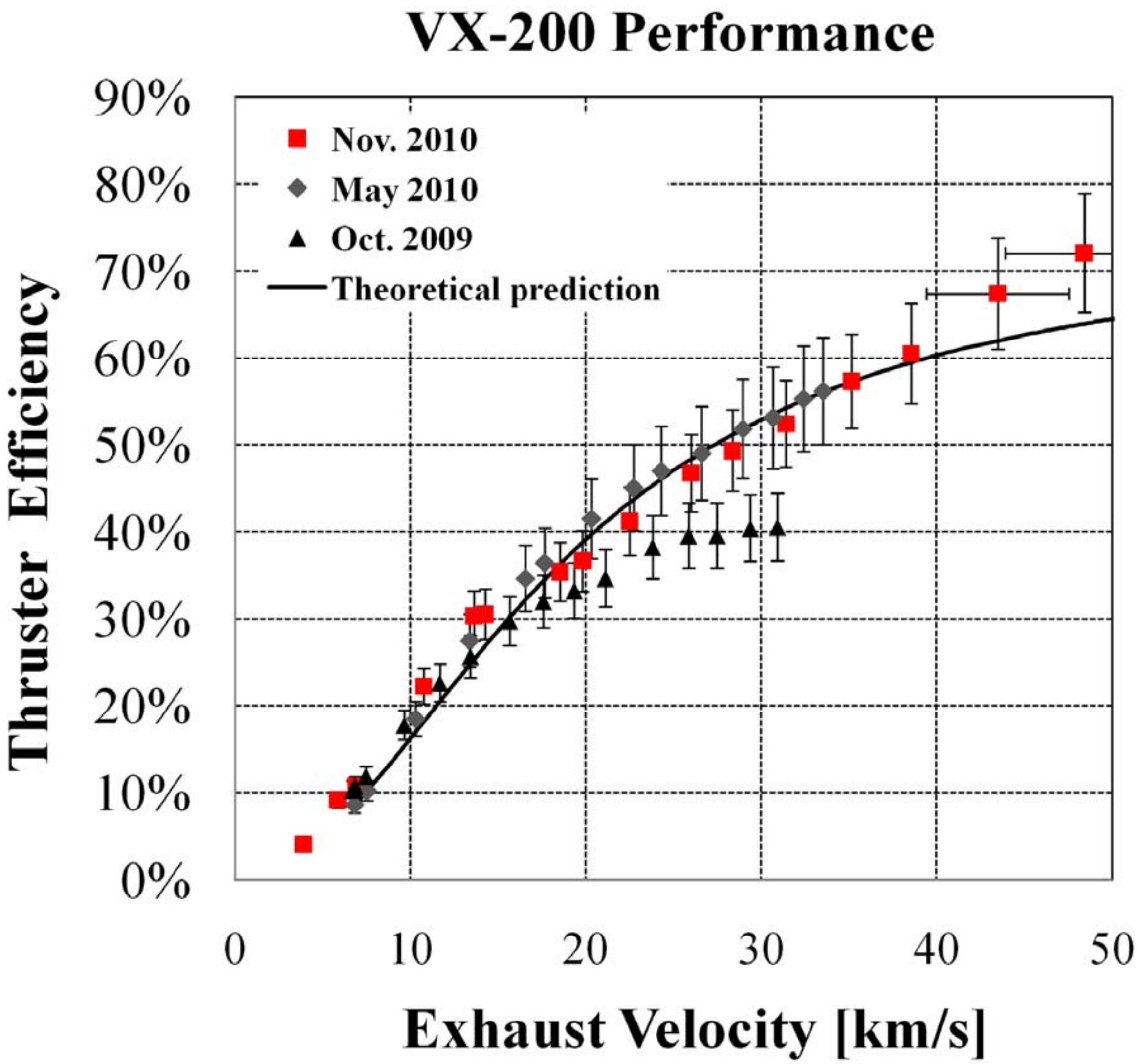

Figure 23. Thruster efficiency vs exhaust velocity (specific impulse x 10). Results are shown for three separate experimental campaigns in October 2009, May of 2010 and November of 2010. Hardware refinements to the second stage have led to significant performance improvement.

VII. References

[1] K. Sankaran, L. Cassady, A. D. Kodys et al., "A survey of propulsion options for cargo and piloted missions to Mars." Presented at the *International Conference on New Trends in Astrodynamics,* Jan. 20-22, 2003 (unpublished).

[2] F. R. Chang-Díaz, "Fast, power-rich space transportation, key to human space exploration and survival." Presented at the *53rd International Astronautical Congress / The World Space Congress,* 10-19 Oct 2002, Houston, Texas, 2002.

[3] E. A. Bering III, F. R. Chang-Díaz, and J. P. Squire, "Use of RF waves in space propulsion systems, The" *Bulletin of Radio Science (310),* 92-106 (2004).

[4] R. Frisbee, "SP-100 Nuclear Electric Propulsion for Mars Cargo Missions," *29th AIAA/SAE/ASME/ASEE Joint Propulsion Conference,* Monterey, CA, USA, June 1993, AIAA-93-2092.

[5] R. Frisbee, "Electric Propulsion Options for Mars Cargo Missions," *32nd AIAA/ASME/SAE/ASEE Joint Propulsion Conference and Exhibit,* Lake Buena Vista, FL, USA, July 1996, AIAA-96-3173.

[6] A. Ilin, Cassady, L., Glover, T., Carter, M., and Chang Díaz , F., “A Survey of Missions using VASIMR for Flexible Space Exploration," Tech. Rep. JSC-65825, NASA - JSC, April 2010.

[7] R. W. Boswell and F. F. Chen, "Helicons - The early years." *IEEE Transactions on Plasma Science, 25*(6), 1229-1244 (1997).

[8] F. F. Chen and R. W. Boswell, "Helicons - The past decade." *IEEE Transactions on Plasma Science, 25*(6), 1245-12457(1997).

[9] T. G. Northrop, "The Adiabatic Motion of Charged Particles," *American Journal of Physics, Volume 32,* Issue 10, pp. 807-807 (1964).

[10] J. G. Roederer., *"Dynamics of geomagnetically trapped radiation,"* Physics and Chemistry in Space, Berlin: Springer, 1970.

[11] E. A. Bering III, Chang Díaz,F.R., Squire,J.P., Glover, T.W., Carter, M.D., McCaskill, G.E., Longmier, B.W., Brukardt, M.S., Chancery, W.J., Jacobson, V.T., "Observations of single-pass ion cyclotron heating in a trans-sonic flowing plasma," *Physics of Plasmas 17,* 043509, 2010.

[12] F. R. Chang-Díaz and J. L. Fisher, “A supersonic gas target for a bundle divertor plasma.” *Nuclear Fusion 22*(8), 1982.

[13] F. R. Chang Díaz, "Research status of the Variable Specific Impulse Magnetoplasma Rocket," presented at the *39th Annual Meeting of the Division of Plasma Physics,* 1997 (unpublished).

[14] F. R. Chang Díaz, "Research Status of the Variable Specific Impulse Magnetoplasma Rocket," presented at the *Open Systems,* July 27-31, 1998, Novosibirsk, Russia, 1998 (unpublished).

[15] F. R. Chang Díaz, J. P. Squire, A. V. Ilin et al., "Development of the VASIMR™ Engine, The," presented at the *International Conference of Electromagnetics in Advanced Space Applications,* Sep 13-17, 1999, Torino, Italy, 1999 (unpublished).

[16] F. R. Chang Díaz, J. P. Squire, E. A. Bering III et al., "VASIMR™ Engine Approach to Solar System Exploration, The," presented at the *39th AIAA Aerospace Sciences Meeting and Exhibit,* Jan. 8-11, 2001, Reno, NV, 2001.

[17] F. R. Chang Díaz, J. P. Squire, T. Glover et al., "VASIMR™ Engine: Project Status and Recent Accomplishments, The," presented at the *42nd AIAA Aerospace Sciences Meeting and Exhibit,* Reno, NV, 2004.

[18] N. J. Fisch, "Confining a tokamak plasma with rf-driven currents," *Physical Review Letters, 41*(13), 873 (1978).

[19] S. N. Golovato, K. Brau, J. Casey et al., "Plasma Production and Heating in a tandem mirror central cell by radio frequency waves in the ion cyclotron frequency range," *Phys. Fluids, 3* (12), 3744-3753 (1988).

[20] Y. Yasaka, R. Majeski, J. Browning et al., "ICRF heating with mode control provided by a rotating field coupler," *Nuclear Fusion, 28,* 1765 (1988).

[21] D.G. Swanson, *Plasma Waves* (Academic Press, Boston, 1989).

[22] T. H. Stix, *Waves in Plasma* (American Institute of Physics, New York, NY, 1992).

[23] E. A. Bering III, M. Brukardt, F. R. Chang-Díaz et al., "Experimental studies of the exhaust plasma of the VASIMR™ engine." Presented at the *40th AIAA Aerospace Sciences Meeting and Exhibit,* Reno, NV, 2002.

[24] E. A. Bering III, M. S. Brukardt, W. A. Rodriguez et al., "Ion Dynamics and ICH Heating in the Exhaust Plasma of The VASIMR™ Engine." Presented at the *53rd International Astronautical Congress / The World Space Congress,* 10-19 Oct., Houston, Texas, 2002.

[25] D. G. Chavers and F. R. Chang-Díaz, "Momentum flux measuring instrument for neutral and charged particle flows." *Rev. Sci. Instrum., 73*(10), 3500-3507 (2002).

[26] B. N. Breizman and A. V. Arefiev, "Single-Pass Ion Cyclotron Resonance Absorption." *Physics of Plasmas, 8*(3), 907-915 (2001).

[27] E. G. Shelley, R. D. Sharp, and R. G. Johnson, "Satellite observations of an ion acceleration mechanism." *Geophysical Research Letters, 3*(11), 654 (1976).

[28] R. D. Sharp, R. G. Johnson, and E. G. Shelley, "Observation of an ionospheric acceleration mechanism producing energetic (keV) ions primarily normal to the geomagnetic field direction." *Journal of Geophysical Research, 82*, 3324 (1977).

[29] F. S. Mozer, C. W. Carlson, M. K. Hudson et al., "Observations of paired electrostatic shocks in the polar shocks in the polar magnetosphere." *Physical Review Letters, 38,* 292 (1977).

[30] A. G. Ghielmetti, R. G. Johnson, R. D. Sharp et al., "The latitudinal, diurnal and altitudinal distributions of upward flowing energetic ions of ionospheric origin." *Geophysical Research Letters, 5,* 59 (1978).

[31] E. G. Shelley, "Heavy ions in the magnetosphere." *Space Science Reviews, 23,* 465 (1979).

[32] R. D. Sharp, R. G. Johnson, and E. G. Shelley, "Energetic particle measurements from within ionospheric structures responsible for auroral acceleration processes." *Journal of Geophysical Research, 84,* 480 (1979).

[33] H. L. Collin, R. D. Sharp, E. G. Shelley et al., "Some general characteristics of upflowing ion beams over the auroral zone and their relationship to auroral electrons." *Journal of Geophysical Research, 86,* 6820 (1981).

[34] M. Zintl, R. McWilliams, and N. Wolf, “Transverse ion acceleration and ion conic formation in a divergent-field laboratory plasma.” *Physics of Plasmas, 2* (12), 4432-4441 (1995).

[35] M. André, P. Norqvist, L. Andersson, L. Eliasson, A.L. Eriksson, L. Blomberg, R. Erlandson, and J. Waldemark, “Ion energization mechanisms at 1700 in the auroral region.” *Journal of Geophysical Research, 103* (A3), 4199-4222 (1998).

[36] J. M. Kindel, and C.F. Kennel, “Topside current instabilities.” *Journal of Geophysical Research, 76,* 3055 (1971).

[37] E. Ungstrup, D.M. Klumpar, and W.J. Heikilla, “Heating of ions to superthermal energies in the topside ionosphere by electrostatic ion cyclotron waves.” *Journal of Geophysical Research, 84,* 4289 (1979).

[38] M. Ashour-Abdalla, H. Okuda, and C. Cheng, "Acceleration of heavy ions on auroral field lines." *Geophysical Research Letters, 8,* 795-798 (1981).

[39] T. Chang, G.B. Crew, N. Hershkowitz, J.R. Jasperse, J.M. Retterer, and J.D. Winningham, "Transverse acceleration of oxygen ions by electromagnetic ion cyclotron resonance with broad band left-hand polarized waves." *Geophysical Research Letters, 13* (7), 636-639 (1986).

[40] R. E. Erlandson, L.J. Zanetti, T.A. Potemra, M. André, and L. Matson, "Observation of electromagnetic ion cyclotron waves and hot plasma in the polar cusp." *Geophysical Research Letters, 15,* 421 (1988).

[41] R. E. Erlandson, L.J. Zanetti, M.H. Acuna, A.I. Eriksson, L. Eliasson, M. Boehm, and L.G. Blomberg, "Freja observations of electromagnetic ion cyclotron ELF waves and transverse oxygen ion acceleration on auroral field lines." *Geophysical Research Letters, 21* (17), 1855-1858 (1994).

[42] J. E. Borovsky, "The production of ion conics by oblique double layers." *Journal of Geophysical Research, 89* (A4), 2251-2266 (1984).

[43] R. McWilliams, and R. Koslover, "Laboratory observation of ion conics by velocity space tomography of a plasma." *Physical Review Letters, 58* (1), 37-40 (1987).

[44] E. A. Bering III, M. C. Kelley, and F. S. Mozer, "Observations of an intense field aligned thermal ion flow and associated intense narrow band electric field oscillations." *Journal of Geophysical Research, 80* (34), 4612-4620 (1975).

[45] E. A. Bering III and M. C. Kelley, "Observation of Electrostatic Ion Cyclotron Waves at the Boundary of an Auroral Arc." *EOS, Transactions, American Geophysical Union, 56,* 173 (1975).

[46] M. C. Kelley, E. A. Bering III, and F. S. Mozer, "Evidence that the electrostatic ion cyclotron instability is saturated by ion heating." *Physics of Fluids, 18,* 1590-1597 (1975).

[47] P. M. Kintner, M. C. Kelley, and F. S. Mozer, "Electrostatic hydrogen cyclotron waves near one earth radius altitude in the polar magnetosphere." *Geophysical Research Letters, 5,* 139 (1978).

[48] P. M. Kintner, M. C. Kelley, R. D. Sharp et al., "Simultaneous observations of energetic (keV) upstreaming ions and electrostatic hydrogen cyclotron waves." *Journal of Geophysical Research, 84,* 7201-7212 (1979).

[49] P. M. Kintner, "On the distinction between electrostatic ion cyclotron waves and ion cyclotron harmonic waves." *Geophysical Research Letters, 7,* 585 (1980).

[50] E. A. Bering III, "Apparent Electrostatic Ion Cyclotron Waves in the Diffuse Aurora." *Geophysical Research Letters, 10,* 647-650 (1983).

[51] E. A. Bering III, "The Plasma Wave Environment of an Auroral Arc, 1., Electrostatic Ion Cyclotron Waves in the Diffuse Aurora." *Journal of Geophysical Research, 89,* 1635-1649 (1984).

[52] P. M. Kintner, W. Scales, J. Vago et al., "Harmonic H^+ gyrofequency structures in auroral hiss observed by high-altitude auroral sounding rockets." *Journal of Geophysical Research, 96*(A6), 9627-9638 (1991).

[53] J. Bonnell, P. Kintner, J.E. Wahlund, K. Lynch, and R. Arnoldy, "Interferometric determination of broadband ELF wave phase velocity with a region of transverse auroral ion acceleration." *Geophysical Research Letters, 23* (23), 3297-3300 (1996).

[54] P. M. Kintner, J. Bonnell, R. Arnoldy, K. Lynch, C. Pollock, and T. Moore, "SCIFER – Transverse ion acceleration and plasma waves." *Geophysical Research Letters, 23,* 1873-1876 (1996).

[55] P. M. Kintner, P.W. Schuck, and J.R. Franz, "Spaced measurements and progress in understanding space plasma waves." *Physics of Plasmas, 7* (5), 2135-2141 (2000a).

[56] P. M. Kintner, J. Franz, P. Schuck, and E. Klatt, "Interferometric coherency determination of wavelength or what are broadband ELF waves?" *Journal of Geophysical Research, 105* (A9), 21237-21250 (2000b).

[57] W. E. Amatucci, D.N. Walker, G. Ganguli, D. Duncan, J. Antoniades, J.H. Bowles, V. Gavrishchaka, and M.E. Koepke, "Velocity-shear-driven ion-cyclotron waves and associated transverse ion heating." *Journal of Geophysical Research, 103* (A6), 11711-11724 (1998).

[58] D. L. Correll, H. Boehmer, N. Rynn, and R.A. Stern, "Temporal evolution of ion temperatures in the presence of ion cyclotron instabilities." *Physics of Fluids, 20* (5), 822-828 (1976).

[59] S. Cartier, N. D'Angelo, and R. Merlino, "A laboratory study of ion energization by EIC waves and subsequent upstreaming along diverging magnetic field line." *Journal of Geophysical Research, 91* (A7), 8025-8033 (1986).

[60] A. Fruchtman, "Double layer and thrust." *47th Annual Meeting of the Division of Plasma Physics, Bulletin of the American Physical Society, 50,* pp. 109, Denver, Colorado. (2005).

[61] J. P. Squire, F. R. Chang-Díaz, V. T. Jacobson et al., "Helicon plasma injector and ion cyclotron acceleration development in the VASIMR™ experiment." Presented at the *36th AIAA/ASME/SAE/ASEE Joint Propulsion Conference,* July 17-19, Huntsville, Alabama, 2000.

[62] A. Petro, F. R. Chang-Díaz, A. V. Ilin et al., "Development of a space station-based flight experiment for the VASIMR™ magneto-plasma rocket." Presented at the *40th AIAA Aerospace Sciences Meeting and Exhibit,* 14-17 January, Reno, NV, 2002.

[63] F. R. Chang Díaz, "An overview of the VASIMR™ engine: High power space propulsion with RF plasma generation and heating." Presented at the *14th Topical Conference on Radio Frequency Power in Plasmas,* May 7-9, Oxnard, CA, 2001 (unpublished).

[64] R. W. Boswell, "Very efficient plasma generation by whistler waves near the lower hybrid frequency." *Plasma Phys. Control. Fusion, 26,* 1147 (1984).

[65] F. F. Chen, "Plasma ionization by helicon waves." *Plasma Physics and Controlled Fusion, 33*(4), 339-364 (1991).

[66] R. W. Boswell and F. F. Chen, "Helicons - The Early Years." *IEEE Transactions on Plasma Science, 25*(6), 1229-1244 (1997).

[67] R. W. Boswell and C. Charles, "The helicon double layer thruster." Presented at the *28th International Electric Propulsion Conference, IEPC 2003,* Toulouse, France, 2003.

[68] V. I. Krassovsky, "Exploration of the upper atmosphere with the help of the third Soviet sputnik." *Proc. IRE, 47,* 289 (1959).

[69] E. C. Whipple, "The ion trap-results in "Exploration of the upper atmosphere with the help of the third Soviet sputnik"." *Proc. IRE, 47,* 2023 (1959).

[70] W. B. Hanson and D. D. McKibbin, "An ion-trap measurement of the ion-concentration profile above the F_2 peak." *Journal of Geophysical Research, 66,* 1667 (1961).

[71] L. W. Parker and E. C. Whipple, "Theory of spacecraft sheath structure, potential, and velocity effects on ion measurements by traps and mass spectrometers." *Journal of Geophysical Research, 75,* 4720-4733 (1970).

[72] W. B. Hanson, S. Sanatani, D. Zuccaro et al., "Plasma measurements with the retarding potential analyzer on OGO 6." *Journal of Geophysical Research, 75*(28), 5483-5501 (1970).

[73] W. B. Hanson, R. A. Heelis, R. A. Power et al., "The retarding potential analyzer for Dynamics Explorer-B." *Space Science Instruments, 5,* 503-510 (1981).

[74] S. Minami and Y. Takeya, "Ion temperature determination in the ionosphere by retarding potential analyzer aboard sounding rocket." *Journal of Geophysical Research, 87,* 713 (1982).

[75] B. W. Longmier, A. D. Gallimore, F. R. Chang-Díaz, J. P. Squire, T. W. Glover, D. G. Chavers, E. A. Bering III, and B. M. Reid, Validating a plasma momentum flux sensor with a Hall thruster mounted on an inverted pendulum thrust stand, *J. Prop. Power,* doi: 10.2514/1.35706, 2009.

[76] J. P. Squire, F. R. Chang-Díaz, R. Bengtson et al., "A plasma diagnostic set for the study of a variable specific impulse magnetoplasma rocket." Presented at the *APS Division of Plasma Physics Meeting,* Pittsburg, PA, 1997 (unpublished).

[77] I. H. Hutchinson, *Principles of Plasma Diagnostics* (Cambridge University Press, Cambridge, 1987).

[78] R. L. Stenzel, R. Williams, R. Aguero, K. Kitazaki, A. Ling, T. McDonald, and J. Spitzer, “Novel directional ion energy analyzer.” *Review of Scientific Instruments, 53* (7), 1027-1031 (1982).

[79] R. L. Stenzel, W. Gekelman, N. Wild, J.M. Urrutia, and D. Whelan, “Directional velocity analyzer for measuring electron distribution functions in plasma.” *Review of Scientific Instruments, 54*, 1302-1310 (1983).

[80] L. D. Cassady, Longmier, B.W., Olsen, C.S., Ballenger, M.G., McCaskill, G.E., Ilin, A.V., Carter, M.D., Glover, T.W., Squire, J.P. , Chang Díaz, F.R., “VASIMR Performance Results,” AIAA Paper 2010-6772, *46th AIAA/ASME/SAE/ASEE Joint Propulsion Conference & Exhibit,* Nashville, TN, 25-28 July, 2010.

[81] W. Cox, C. Charles,R. Boswell, and R. Hawkins, Spatial retarding field energy analyzer measurements downstream of a helicon double layer plasma, *Appl. Phys. Lett., 93,* 071505 2008.

[82] G. Sutton and O. Biblarz, *Rocket Propulsion Elements,* 7th edition, John Wiley & Sons, Inc., 2001.

[83] Ilin, A., Chang Díaz , F., Squire, J., Tarditi, A., Breizman, B., and Carter, M., “Simulations of Plasma Detachment in VASIMR," *40th AIAA Aerospace Sciences Meeting and Exhibit ,* Reno, NV, January 14-17 2002, AIAA 2002-0346.

[84] Arefiev, A. and Breizman, B., “Magnetohydrodynamic scenario of plasma detachment in a magnetic nozzle," *Physics of Plasmas, Vol. 12,* 2005

[85] H. Böhrk and M. Auweter-Kurtz, Thrust measurement of the hybrid electric thruster TIHTUS by a baffle plate, *J. Propulsion Power Vol. 25,* No. 3, pp. 729-736, 2009.

[86] B. W. Longmier , L. D. Cassady, M. G. Ballenger, M. D. Carter, F. R. Chang Díaz, T. W. Glover, A. V. Ilin, G. E McCaskill, C. S. Olsen, J. P. Squire, E. A. Bering, III, “VX-200 Magnetoplasma Thruster Performance Results Exceeding 50% Thruster Efficiency,” , *J. Prop. Power,* 2010, (in press).